Organic diagenesis in stromatolitic dolomite and chert from the late Palaeoproterozoic McLeary Formation

Nadine W. Gabriel[1,2], Dominic Papineau[1,3,4,5], Zhenbing She[5,6], Arne Leider[7,8], and Marilyn L. Fogel[9]

1 Department of Earth Sciences, University College London, United Kingdom

2 Department of Earth Sciences, Natural History Museum, London, United Kingdom

3 London Centre for Nanotechnology, University College London, United Kingdom

4 Centre for Planetary Sciences, University College London & Birkbeck College London, United Kingdom

5 State Key Laboratory of Biogeology and Environmental Geology, China University of Geosciences, Wuhan, China

6 School of Earth Sciences, China University of Geosciences, Wuhan, China.

7 MARUM, Center for Marine Environmental Sciences, University of Bremen, Germany

8 Max-Planck-Institute for Biogeochemistry, Jena, Germany

9 Department of Earth and Planetary Sciences, UC Riverside, California, United States of America

Abstract

Extensive stromatolitic carbonate platforms developed during and after the Palaeoproterozoic Great Oxidation Event (GOE), which records a significant increase of oxygen in the atmosphere and oceans. Stromatolites link biological and non-biological processes through their microscopic organo-sedimentary structures that have the potential to provide information about microbial and diagenetic processes that operate during their formation. This study aims to document the mineralogy and organic geochemistry of microscopic diagenetic structures in the exceptionally-preserved late Palaeoproterozoic stromatolitic dolomite from the McLeary Formation of the Belcher Islands, in Nunavut, Canada. This is done to test the hypothesis that chemically oscillating reactions can influence the formation of diagenetic spheroids such as rosettes, granules, concretions, and botryoids; these reactions occur over short timescales during diagenesis, i.e. before the lithification of the sediment. Decimetre-size columnar stromatolites from the McLeary Formation contain centimetre-size pyrite concretions, which themselves also contain framboids. Inside rounded, black chert concretions and coarse quartz granules, there are filamentous microfossils composed of organic matter partly replaced by pyrite. These observations are consistent with post-depositional oxidation-reduction reactions involving organic matter and sulphate. In comparison, decimetre-size tabular bioherms of millimetre-to-centimetre size stromatolite columns contain microscopic dolomitic carbonate structures including circularly-concentric rosettes, zoned dolomite rhombs, and cavity structures of rounded equidistant laminations, all of which are layered with organic matter. All these diagenetic spheroids co-occur with circularly-concentric, equidistant and laminated minerals associated with degraded organic matter or microfossils. The composition and geometry of these features are consistent with the non-biological oxidation of biological carboxylic acids during diagenetic chemically

oscillating reactions. Hence, both biological and non-biological processes play a major role in the precipitation of diagenetic spheroids in McLeary stromatolites. Increased abundance of organic matter as microbial biomass, as well as oxidised halogens and sulphate, led to widespread organic decomposition in the Palaeoproterozoic McLeary Formation. Ultimately, chemically oscillating reactions after periods of oxygenation likely play a more significant role than previously thought in the formation of diagenetic spheroids inside stromatolitic dolomite.

1. Introduction

Stromatolites are laminated, organo-sedimentary mounds or columns that have been present in the rock record for over three billion years. Structures in dolomitic rocks of the 3.7 Ga old Isua supracrustal belt in Southwest Greenland have been interpreted as domal and conical dolomitic stromatolites by ***Nutman et al. (2016)***. However, this has been contested by ***Allwood et al. (2018)*** who suggested that they are deformation structures. While the solution to this debate awaits further correlated microscopic analyses, there are convincing examples of Palaeoarchaean stromatolites, including the domal and conical forms from the 3.48 Ga old Dresser Formation in Pilbara Craton, Western Australia ***(Djokic et al., 2017)*** and in the contemporary 3.3–3.5 Ga old Barberton Greenstone belt in South Africa ***(Byerly et al., 1986; Homann, 2019)***.

Stromatolites form in shallow-marine environments and are built up by trapping and binding sediment by mucilage secreting microorganisms and/or the precipitation of minerals ***(Walter, 1976)***. Additionally, ecophysiological, biophysical and hydrodynamic processes play an important role in stromatolite growth, that can be grouped into intrinsic (e.g. microbial growth, biostabilisation, mineral precipitation, and the production of biopolymers) and

extrinsic (e.g. seawater chemistry, sedimentation/burial rate, and wave motion) factors ***(Bosak et al., 2013; Hickman-Lewis et al., 2019)***.

The active surface of a stromatolite consists of a microbial mat, that encompasses generations of adhesive, extracellular polymeric substance (EPS)-bonded microbial communities. Over time, mineral particles become bound and incorporated into the mat when later generations of microorganisms grow over them ***(Frantz et al., 2015)***; the permineralisation of microbial mats form stromatolite laminae. This accretion can only occur if the the balance between sediment supply and mat destruction by shear and abrasion is perfect, and if the lithified structure is strong enough to withstand turbulent shear ***(Reid et al., 2000; 2003)***. Some of the microorganisms responsible for the formation of stromatolites are photoautotrophs, such as cyanobacteria and anoxygenic phototrophs, that have been reported to be concentrated in the topmost millimetre of modern stromatolites in Hamelin Pool in Shark Bay, Western Australia ***(Papineau et al., 2005)***.

The diverse range of stromatolites in the late Palaeoproterozoic McLeary Formation (Belcher Islands, Canada) provides an opportunity for an in-depth petrographic study, because these stromatolites are well-preserved and exposed in the Belcher Islands, and have not been subjected to significant thermal metamorphism. Stromatolites are often associated with spheroids, but the relationship between the two is poorly documented. The origin of spheroids could be from gas bubble formation ***(e.g. Bosak et al., 2010)*** or other diagenetic reactions. Diagenetic spheroids are a group of sub-rounded mineral structures that include concretions, granules, rosettes, and botryoids ***(Papineau et al., 2016; 2017; Dodd et al., 2018; Papineau, 2020)***. They are sub-ellipsoidal mineral structures that may exhibit concentric layering and are typically composed of microcrystalline quartz, dolomite, pyrite, and/or apatite. Concretions, granules and rosettes can be distinguished on the basis of their sizes:

respectively greater than a few millimetres, a few millimetres to ~200 µm, and less than ~200 µm. Botryoids can range from micron to decimetre sizes. Their patterns are similar to those generated in experiments conducted by ***Papineau (2020)***, with randomly localised epicentres of concentric chemical waves, where oxidation spots begin to emit the radially-expanding circular waves of reaction products. Similarly, patterns formed by chemically oscillating reactions form mathematical fractals because the chemical waves destructively interfere when they meet, occur over three size dimension scales and oscillate over at least three time dimension scales in experiments ***(Papineau, 2020)***. This latest work further suggests that these experimental morphological features are also geometrically similar and compositionally analogous to those of supergene malachite botryoids from the Congo, for instance. Hence, it is important to carefully assess the possibility that morphologically similar features in dolomitic stromatolite formations may represent the patterns of abiotic chemically oscillating reactions during the diagenetic oxidation of organic matter, since there are also other possible processes for their formation.

Because spheroids sometimes occur with current-generated structures, another common explanation for their origin has been wave action in a high-energy, shallow-marine environment ***(Simonson, 2003; Pufahl & Fralick, 2004; Lascelles, 2007; Akin et al., 2013; Smith et al., 2017)***. In fact, the concentric and radial morphology of some diagenetic spheroids is similar to carbonate oolites from shallow-marine, wave-agitated waters ***(Brehm et al., 2003; Pacton et al., 2012; Flannery et al., 2019)***. When spheroids occur in microbial mats and stromatolites, they have alternatively been interpreted as gas bubbles produced by oxygenic phototrophs ***(Bosak et al., 2010)***. These models of wave action and bubbles, however, do not fully explain the association of spheroids with stromatolites, as well as their circularly-concentric layering and acicular radiating mineral habits, organic matter contents, and the

frequent occurrence of micro-fossils within them. The bubbles reported by ***Bosak et al. (2010)*** also lack internal features (mineral inclusions, organic matter, etc.). Examples attributed to chemically oscillating reactions include, among others, diagenetic spheroids in chert granules ***(Papineau et al., 2017)***, granular iron formations ***(Dodd et al., 2018)***, rosettes in phosphorites ***(Papineau et al., 2016)***, and malachite botryoids ***(Papineau, 2020)***.

Chemically oscillating reactions represent a possible formation mechanism for diagenetic spheroids in stromatolitic dolomite. One type of chemically oscillating reaction is the Belousov-Zhabotinsky (BZ) reaction that involves the out-of-equilibrium oxidation of carboxylic acids (-COOH) with an oxidiser and its corresponding halide salt, and sulphate, and which produces concentric and radial geometric patterns ***(Zaikin & Zhabotinsky, 1970; Papineau, 2020)***. Such organic acids could include amino acids and phospholipids in cell membranes and they are also common in metabolites in biochemical cycles. Therefore, metabolically-active microbial communities that form stromatolites could readily provide these key compounds. Chemically oscillating reactions could occur in the early diagenetic environment when organic acids produced by the breakdown of organic matter are oxidised ***(Papineau et al., 2017; Papineau, 2020)***.

The hypothesis then arises that chemically oscillating reactions could potentially facilitate mineral precipitation in stromatolites because the CO_2 produced before dolomitisation can react with Ca^{2+} and Mg^{2+} to form protodolomite, especially in the presence of EPS ***(Liu et al., 2019a)***. However, the low pH of the BZ reaction (around 2) is not immediately conducive to carbonate precipitation. For the BZ reaction to occur spontaneously, sulphate and halogens, including oxidised halogens, should have been present in the diagenetic environment of the McLeary Formation, and the pH would have required some alkalinity to

precipitate chert, carbonate, or apatite. Pyritisation could have been favoured by sulphate-bearing diagenetic pore waters as sites for biomass decarboxylation.

However, some spheroids have characteristics consistent with all models including microbial activity and wave agitation, in addition to diagenetic reactions such as chemically oscillating reactions ***(Dodd et al., 2018)***. The presence of mineral assemblages that commonly include apatite, ^{13}C-depleted carbonate, chert, sulphide, and organic matter is most consistent with an origin from the diagenetic oxidation of biomass. Therefore, to test the respective contributions from the different mechanisms inside stromatolitic dolomite, we provide new descriptions of diagenetic structures in the well-preserved McLeary stromatolite, and document the mineral associations with organic matter. The documentation of the minerals that arise from from the above-mentioned processes is important to identify possible indirect biosignatures, or sedimentological evidence for carbon cycling in dolomitic-cherty stromatolites, which has implications for understanding the fossil record of stromatolites in deep time.

2. Geological setting and sample material

During the Neoarchaean, the supercontinent called Kenorland comprised cratons from North America, Fennoscandia and the Siberian Shield ***(Williams et al., 1991)***. Kenorland began to break up around 2.5 Ga ago, which lead to the formation of an intracontinental ocean between 2.2 and 2.06 Ga ago ***(Melezhik & Hanski, 2012)***, but these continental fragments were reassembled again between 1.9 and 1.8 Ga ago during the Trans-Hudson Orogeny ***(Rogers & Santosh, 2004)***, which formed the supercontinent Nuna ***(Bleeker, 2003)***. The resulting Trans-Hudson Orogen is 4600 km long and 800 km wide and stretches from the centre to the northeast of North America ***(Figure 1A; St-Onge et al., 2007)***. It separates the

underthrust Superior Craton from the Archaean crustal blocks, which are comprised of the Wyoming, Hearne, Rae, Superior and Slave Cratons ***(Bleeker, 2003; St-Onge et al., 2007)***. The Superior Craton has a cratonisation age of 2.68–2.63 Ga and is dominantly composed of tonalite-trondhjemite-granodiorite ***(Bleeker, 2003)***, but the contact of the Belcher Group with this basement has not yet been documented.

The Belcher Islands are located on a section of the Trans-Hudsonian Orogen called the Circum-Superior Belt, which consists of oceanic basalts and sedimentary rocks ***(Arndt & Todt, 1994)***. Uranium-lead dating on zircons carried out by ***Hodgkiss et al. (2019)*** shows that the maximum age of the Belcher Group is 2.0185 ± 0.001 Ga (obtained from tuff in the Kasegalik Formation), and the minimum age is 1.8542 ± 0.001 Ga (obtained from the contact between the Flaherty and Omarolluk Formations). The 14 formations of the Belcher Group, including two volcanic units, have a total thickness of 7000–9000 m ***(Figure 1B; Ricketts, 1979)***. The Himalayan-style Trans-Hudson Orogeny is thought to have caused the formation of the anticlines and synclines in the Belcher Islands ***(Figure 1C; Weller & St-Onge, 2017)***.

The names of the formations were first assigned by ***Dimroth et al. (1970) (Table 1).*** These units were deposited during four megacycles that represent changes in the depositional environment ***(Ricketts, 1979)***. During the first megacycle, over a kilometre of carbonates and mudstones of the Kasegalik Formation was deposited in a supratidal environment on a marine platform. The second megacycle began by the emplacement of Eskimo Formation basalts. During this cycle, extensive subsidence led to the deposition of thick sequences of carbonate and clastic sediments, and these formations, including the Fairweather, McLeary, and Tukarak Formations, represent a transgressive platform-slope-basin sequence that developed on a southwest dipping slope. The third megacycle started with the deposition of shallow subtidal and intertidal sandstones of the Mavor Formation, the concretionary green to red mudstones

of the Costello Formation, followed by the mudstone, siltstone, sandstone and chert of the Laddie and Rowatt formations. This megacycle represents a shoaling upwards sequence, which was deposited on a prograding shoreline. The banded ironstones in the Kipalu Formation were deposited under the influence of volcanic activity. Further volcanism occurred at the start of the fourth megacycle with the columnar and pillow basalt of the Flaherty Formation. The erupted material reversed the palaeoslope direction to the east and caused rapid subsidence in the Belcher Basin. This basin was then filled with turbidites and fluvial sediments of the Omarolluk and Loaf formations ***(Ricketts, 1979)***.

A ca. 465 m section through the McLeary Formation was measured on Tukarak Island ***(56°06'N, 78°50'W ; Figure 1D).*** The samples selected for this study mostly derive from a ca. 30 m thick horizon in this section with abundant, well-exposed and exceptionally well-preserved stromatolites characterised by a diverse range of morphologies. The studied horizons are located near the middle and the top of the McLeary Formation ***(Figure 1B)***. The lithologies consist dominantly of grey to pink dolomitic and cherty stromatolites, beige-coloured silty to sandy dolomite, and some dolomitic limestone. Stromatolite morphologies in these horizons include decimetre-size, non-branching domal to turbinate stromatolites and tabular bioherms of centimetre-size, multifurcate and anastomosed stromatolites in chert-rich limestone. Some stromatolites occur with pinching and swelling concretionary structures composed of black chert, such as samples ***BEL-16*** and ***BgMc74bs*** which were collected near the contact with the Tukarak Formation. These samples of the McLeary Formation ***(Table 2)*** are selected for this detailed petrographic study because they contain a representative diversity of stromatolite morphologies.

3. Methods

3.1. Optical microscopy and micro-Raman spectroscopy

Thin sections of 30 µm thickness were made without a cover slip, and polished with 0.25 µm Al_2O_3 powder and deionised water. These thin sections were studied with an Olympus BX51 microscope with 5x, 10x, 20x, 50x and 100x objectives. Both plane- and cross-polarised light were used, and reflected light (bright field) was also used to distinguish between different oxides. Sites of interest were photographed using Stream Start 1.9 software by Olympus Soft Imaging Solutions. These images were then correlated with thin section maps, which were created by scanning thin sections with a flatbed scanner.

Micro-Raman spectroscopy was performed on a WITec Alpha300 Raman microscope with a 532 nm laser at the Department of Earth Sciences, University College London. Objectives of 5x, 10x, 20x, 50x and 100x magnification were used to collect petrographic images, typically with a resolution between 1 and 0.36 µm per pixel. A 50 µm diameter optic fibre was used as a pinhole to achieve a compromise between confocality and signal intensity, whereas a 600 groves/mm grating was used to provide spectra with a wavenumber resolution around 4 cm^{-1} over a bandwidth of 4000 cm^{-1}. All scans were carried out at 1000x magnification with a resolution of one spectrum pixel per micrometre and a scan depth of 1–5 µm below the thin section surface. WITec Project Four Plus software was used to map the peak intensity for different unique molecular bonds in minerals and this was then converted into a colour-coded hyperspectral map. For small mineral grains and fluid inclusions, single spectral analyses were obtained using the 100x objective.

3.2. Scanning electron microscopy (SEM)

A JEOL JSM-6480LV scanning electron microscope with an Oxford Instrument electron dispersive spectrometer (EDS) was used at the Department of Earth Sciences, University College London. After micro-Raman analyses, thin sections were coated with a ~5 nm layer of gold by placing them in a sealed drum with an argon atmosphere and a ~18 mA current for 120 seconds. The coated thin sections were then secured to a sample stage with carbon tape to ensure conductivity and placed in the SEM for observation with a 15 keV electron beam and a working distance of ~70 mm. X-ray radiation was detected with the EDS 80 mm^2 silicon drift detector. Detection of characteristic x-ray emissions from the sample was done by EDS, which was used to quantitively detect elements and provide independent confirmation of mineral assignments. ZAF correction was applied to minimise the effects of atomic absorption and fluorescence excitation, and the analyses were accurate to within ~1 %. All analyses are automatically normalised to 100%.

3.3. Stable isotope geochemistry of organic matter and carbonate

Organic carbon isotope analyses were performed on about 25 mg of micro-drilled powders, which were first acidified with 6N HCl (Sequanal Grade, Pierce) rinsed with deionised water, and then dried. Resulting powders were then analysed in a Costech Elemental Analyzer coupled to a Delta V Advantage isotope ratio mass spectrometer via a Conflo IV interface at the University of California Riverside. Nitrogen levels were at or below the detection limit. Organic carbon concentrations ranged from 0.04 to 5 % carbon, whereas isotope compositions were determined relative to laboratory standard compounds (acetanilide ($\delta^{13}C$ = -33.69‰; n = 5) and glycine ($\delta^{13}C$ = -36.57‰; n = 2)) and a rock powder (SDO-1 ($\delta^{13}C$ = -30.0‰; n = 2)),

259 which had been calibrated relative to international standards and gives an average 1-sigma
260 reproducibility of 0.2‰.

261 Carbonate carbon and oxygen isotopes were measured in about 100–500 μg of whole-
262 rock powders obtained from the same rock chip as the thin sections. A Gas Bench connected
263 to a ThermoFinnigan Delta V Advantage IRMS, also in continuous flow was used for these
264 analyses. Bulk rock powders inserted in exetainer vials were reacted overnight with 99.9 %
265 pure phosphoric acid at 70 °C. Analyses of carbonate standards NBS 18, NBS 19, and two in-
266 house calcite and dolomite standards were also performed. Reproducibility for carbonate
267 carbon and oxygen isotope analyses was ± 0.12 ‰ and values are reported with respect to
268 PDB and SMOW.

269

270 ## 4. Results

271 ### 4.1. Stromatolite morphology and petrography

272 A range of macroscopic to microscopic mineralogical and organo-sedimentary features
273 is documented in two major stromatolite morphotypes based on the stromatolite
274 classification system by ***Walter et al. (1992)***: 1) the decimetre-size non-branching columnar
275 to domal cherty stromatolites, and 2) tabular bioherms of centimetre-size multifurcate,
276 turbinate and anastomosed stromatolites ***(Figure 2 and 3)***. ***Figure 3*** shows the locations of
277 the microscopic features in this study in their petrological and sedimentological context of the
278 studied McLeary stromatolite thin sections.

279 In outcrops, the stromatolites of the McLeary Formation are decimetre- to centimetre-
280 size with a range of columnar morphologies ***(Figure 2)***. Some stromatolites are 4–20 cm wide,
281 domal to turbinate and columnar non-branching, and some have an elongate horizontal cross
282 section ***(Figures 2A–D)***. Higher up in the studied horizon, stromatolite columns exhibit

generally smaller diameters of between 1 mm to 1 cm, have bifurcate to multifurcate branching, and are arranged as tabular bioherms of coalesced to anastomosed centimetre-size stromatolites ***(Figures 2E–F)***. Above this, stromatolites are hemispherical and up to 10–30 cm wide, or they are 50 cm wide with hemispherical, turbinate or bulbous forms. These turbinate and bulbous stromatolites have multifurcate branching and sometimes possess decimetre-size black chert concretions at their base ***(Figures 2G–H)***. All stromatolites have convex-upward laminae, which are clearly visible in plane-polarised light due to laminations with variable levels of kerogen; this produces alternating light and dark layers in chert and micritic carbonate ***(Figure 3)***. In thin section, laminated silty dolomite is rich in outsized quartz crystals ***(BgMc11034, Figure 3A)*** and contain millimetre-size dolomite granules. Decimetre-size domal to turbinate stromatolites a few metres above contain pyrite layers and centimetre-size pyrite-rich concretions, microscopic stylolites and microbial mat-like wrinkly layers ***(BgMc11035, -36, -37, (Figures 3B–D)***.

In comparison, tabular bioherms of multifurcate to anastomosed centimetre-size stromatolites occur in chert-rich dolomitic carbonate rocks, and co-occur with chert concretions and fine laminations of chert and dolomite ***(BgMc11041, Figures 3E–H)***. Some thin sections show stromatolite morphologies that are visible to the naked eye and at microscopic scales. Thin section ***BgMc11041(1)*** shows the greatest morphological diversity, with millimetre-size turbinate stromatolites along with bifurcate to multifurcate branching forms ***(Figure 3E)***. In some cases, the stromatolite columns are coalesced as two separate stromatolite columns join together, or anastomosed when a stromatolite column separates then re-joins. Stylolites cut across these stromatolite columns and their laminae. In contrast, thin section ***BgMc11041(2) (Figure 3F)*** shows no visible stromatolite morphologies, but there are common calcite veins that cut across wrinkly layers. ***BgMc11041(3)*** and ***-(5) (Figures 3G–***

H) show stromatolites darkened by concentrations of organic matter, which contain millimetre-size turbinate stromatolites, including with bifurcate branching, and the latter contains millimetre-size kerogen clumps.

Some cherty domal stromatolites have millimetre-size clumps of chert-carbonate rich in black kerogen, which form layers of wrinkly filaments that extend over several centimetres ***(BEL11-16, Figure 3I)***. Chert between this black kerogen is clearer and contains less disseminated kerogen. In other domal cherty stromatolites, dark kerogen-rich layers have sub-millimetre protruding kerogenous structures that partly fill the clearer chert interlayers ***(BgMc74bs, Figure 3J)***. These protruding structures have stromatolite-like shapes, but their morphologies are highly irregular.

4.2. Matrix petrography

In many stromatolites, lighter and darker laminae are present showing a thickness of a few tens of micrometres, with the former dominated by chert and the latter being richer in kerogen ***(Figures 4A–D)***. Some laminae are composed of colourless chert, which also forms lenses with an isopachous texture in the micrite ***(Figures 4E–F)***. Alternatively, the matrix is dominated by micritic dolomite as the crystal size is generally less than 4 µm ***(Figure 4E–H)***. The matrix in other samples consists of well-mixed carbonate with chert, both with variable crystal size ***(Figures 4C–D, 4I–J)***. In general, the micritic carbonate matrix is medium to dark grey, however sparry carbonate (crystal size greater than 50 µm) is pale grey or colourless. Occasionally, the carbonate matrix possesses 100–500 µm thick laminations ***(Figures 3B–D, 3J)***, which are either the result of changes in grain size, colour, the presence of organic matter in varying density, or the amount of pyrite present. Carbonate is also found as >200 µm large crystals inside millimetre-long lenses that cut across the micritic carbonate matrix and wrinkly

layers ***(Figures 4G–H)***. There are also chert lenses that cut across isopachous quartz and masses of chert ***(Figures 4I–J)***.

In stromatolites with centimetre-tall, millimetre-wide, multifurcate to anastomosed, and turbinate morphologies ***(Figures 3G–H)***, coarse-grained chert occurs as isopachous quartz that fills cavities between millimetre-size kerogen-rich masses of chert in the matrix ***(Figures 4C–D, 4I–J)***. These chert masses often contain groups of organic-rich microscopic coccoid-like structures at their epicentre ***(Figure 4I)***. The fan-like texture of isopachous quartz is only visible in cross-polarised light ***(Figure 4J)*** and the isopachous quartz cavities are occasionally rimmed by a thin layer of micritic carbonate ***(Figures 4C–D)***.

In most instances, quartz is found as outsized grains either scattered throughout the matrix ***(Figure 3A)*** or at the root of millimetre-tall turbinate stromatolites ***(Figures 4A–B)***. Some outsized quartz crystals can reach up to 700 µm in size and can contain various inclusions such as pyrite, haematite, anatase, kerogen, and fluids. Thin section ***BgMc11041(2)*** shows a ~200 µm wide quartz crystal with several segmented filamentous structures and fluid inclusions throughout the crystal ***(Figure 5A)***. The quartz crystals that contain these filaments occur between organic-rich, wrinkly layers which bear a resemblance to microbial mat layers ***(Figure 3F)***. The filaments are 25–70 µm long, 4–6 µm wide, and consist of well-organised trails of smaller, slightly coiled, segmented, tabular structures ***(Figures 5B–D)***, which co-occur with fluid inclusions ***(Figure 5E)***. In plane-polarised light, the filaments are slightly translucent and brownish-green in colour, but are golden in reflected light, which is consistent with Raman spectra that show they are composed of a mixture of pyrite and kerogen ***(Figure 5F)***. Raman spectra of these kerogen-rich filaments are similar, with typical G-bands around 1601 cm^{-1}, and D1-band peaks around 1343 cm^{-1}. The relative D1/G intensities vary between about 1 and 2.2 ***(Figure 5F; Table 3)***. According to ***Kouketsu et al. (2014)***, these D1/G intensities represent

a metamorphic temperature of 301 to 340 °C. The fluid inclusions in this crystal are mobile under transmitted light illumination and contain a mixture dominated by CO_2 and small amounts of CH_4, as shown by their Raman peaks at 1285 and 1388 cm^{-1}, which are characteristic of CO_2, and 2912 cm^{-1} which represents CH_4 ***(Figure 5F)***.

A second type of filamentous structure composed of kerogen occurs as continuous filaments that form tight sub-aligned groups in chert ***(Figures 5G–I)***. These filaments typically have diameters between about 4 and 6 µm and lengths of over 200 µm and they occur in association with filamentous black kerogen in some cherty domal stromatolites ***(Figure 3I)***. In contrast to the segemented filmanets in ***Figure 5A***, those in ***Figures 5G–I*** are significantly longer, and threadlike with dark edges and a somewhat translucent centre.

Lastly, the third type of coiled filamentous structure occurs inside clumps of dense disseminated kerogen ***(Figure 5J–K)***. This coiled filamentous structure has a diameter of around 20 µm, a length of more than 200 µm, and coil periods of about 20 µm. The coiled filament is also preserved in a halo of clearer chert with a width of about 35 µm. It is composed of finely disseminated black kerogen, distinct from the brown disseminated kerogen of the clumps in which they occur, and are located in the irregular structures protruding from laminations in domal stromatolites ***(Figure 3J)***.

4.3. Chert granules in carbonate

Chert granules are generally common in thin sections that contain centimetre-tall, millimetre-wide multifurcate to anastomosed stromatolites, and these granules occur within a sparry-to-micritic carbonate matrix ***(Figures 6A–B)***. They tend to be rounded, possess a dark brown-grey rim with denser disseminated kerogen, and a relatively clearer centre ***(Figure 6A)***. Cross-polarised light photomicrographs reveal that the rim consists of chert while the

colourless centre contains coarser isopachous quartz, which lack a radial or concentric geometry ***(Figure 6B)***. Other chert granules can contain 200 µm quartz crystals. However, cross-polarised light also reveals that some chert granules do not contain any isopachous or coarse-grained quartz crystals at their centre ***(Figure 6B)***.

Commonly, granules are dark grey, sub-ellipsoidal to elongate structures that are between 200 µm to 1.5 mm in size, and they occur within a matrix of lighter coloured micritic dolomite ***(Figures 6F–G)***. They consist of an amalgamation of outsized quartz and feldspar grains with micron-size grains of rutile and kerogen ***(Figures 6C–D)***. The micritic dolomite within these granules is slightly darker than the surrounding matrix, which imperfectly correlates with variable abundances of disseminated kerogen between the matrix and the granules ***(Figures 6C–D)***. ***Figure 6H*** shows that while kerogen is randomly distributed within the matrix and the micritic granule, quartz and feldspar tends to be more concentrated within the granule. Two Raman spectra of kerogen in granules show variable characteristics with G-bands at 1613 and 1606 cm^{-1}, and D1-bands at 1353 and 1329 cm^{-1}, which suggest possible trace haematite that contaminates the latter peak ***(Figure 6E)***.

4.4. Geometric patterns of organic matter in diagenetic minerals

Mineral grains of carbonate ***(Figures 7A–B)*** and apatite ***(Figures 7C–D)*** are often embedded within micro-stromatolitic chert laminae. In some regions of chert-rich carbonate with wrinkly layers of probable microbial origin, there are microscopic groups of brown, translucent coccoid-like structures up to ~10 µm in diameter ***(Figures 7E–F)***. These microscopic coccoid-like structures composed of kerogen form small clusters less than 100 µm in size. Raman spectra of the kerogen are similar with typical G-bands around 1605 ± 5 cm^{-1} and D1-band peaks around 1344 ± 1 cm^{-1}, which have approximately equal D1/G intensity

ratios ***(Figure 7G)***, and a calculated peak metamorphic temperature of 301 ± 30 °C ***(Lahfid et al., 2010; Kouketsu et al., 2014)***. Highly degraded microscopic spheroids have diffuse outlines ***(Figure 7E)***, and they are sometimes surrounded by equidistant laminations of oriented isopachous quartz crystals, which have varying concentrations of kerogen and co-occur with small grains of rutile and carbonate ***(Figures 8A–F)***. When laminations from more than one cluster of coccoid-like structures combine, they display a pattern similar to the banding seen in agate geodes and BZ patterns, where circular chemical waves destructively interfere, and at the epicentre of this pattern there is a clear, coarser, isopachous quartz infilling ***(Figures 8D–F)***.

There are a number of carbonate structures that are partly composed of kerogen and often possess concentric zonation ***(Figures 8G–J)***. For instance, the carbonate rhomb in ***Figure 8G*** is colourless with a brown translucent core in plane-polarised light. This colour variation does not seem to be the result of disseminated kerogen because the micro-Raman image collected at one micron below the thin section surface shows mostly carbonate ***(Figure 8H)***. Nevertheless, the micro-Raman image reveals two carbonate spectra with similar major peaks but different intensities: the light green carbonate spectrum has a high intensity peak at 1100 cm^{-1} and is found at the edge of the dolomite rhomb, whereas the dark green dolomite spectrum has a high intensity peak at 301 cm^{-1} and is at the centre of the twinned rhomb ***(Figures 8F, 8H)***. In comparison, the carbonate rosettes in ***Figure 8I*** show a correlation between their colour in plane-polarised light and their disseminated kerogen content. They are colourless at the rim and gradually become darker towards the epicentre. The micro-Raman image demonstrates that the pale outer rim is carbonate and the dark epicentre is more kerogen-rich ***(Figure 8I-J)***. These microscopic rosettes are usually less than 200 µm in size, are concentrically layered with kerogen, and have similar dimensions and geometry as

those in contemporaneous phosphatic dolomite from the Michigamme Formation ***(Figure 12p–s in Papineau et al., 2017)***.

Pyrite is also present as euhedral, hexagonal or cubic crystals up to ~120 µm in size. Some crystals possess a translucent, orange rim, probably formed from oxidation after peak metamorphism. All pyrite crystals are poikilitic and tend to be randomly distributed in specific stromatolite layers or in the matrix ***(Figure 3C)***. One sample contains an 8 mm long ellipsoidal pyrite concretion ***(Figure 9A)***, which contains a plethora of smaller pyrite framboids in micritic dolomite ***(Figure 9B)***. Each of these framboids is composed of micron-size sub-hexagonal crystals clustered into a sub-polyhedron shape ***(Figure 9C)***. Pyrite crystals also form discrete layers within the micritic dolomite matrix ***(Figures 3B and 9D)***, which can be discerned by the naked eyes ***(Figure 3D)***. There is an association between iron sulphide minerals and kerogen because pyrite crystals are often found around stylolites ***(Figures 9E–G)***, which usually contain kerogen along with clay and minor amounts of rutile and feldspar ***(Figure 9H)***. Also, pyrite crystals are ~1 µm wide in stromatolites rich in microbial mat-like microstructures, while larger, euhedral pyrite crystals are found in samples devoid of microbial mat-like structures. However, an exception to this rule is that pyrite framboids are often found in close proximity to microbial mat-like structures ***(Figure 3D)***.

Finally, other accessory minerals in the micritic dolomite matrix include small grains of rutile, fluorapatite and microcline, which have been independently detected by micro-Raman and SEM-EDS analyses ***(Figures 10A–B)***. Rutile grains, along with kerogen and an unknown phase with peaks at 446 and 686 cm^{-1} (possibly a phyllosilicate), also occur along the edges of stylolites consisting of carbonate ***(Figures 10C–D)***. Rutile also forms disseminations with anatase, kerogen and feldspar that form an overall acicular shape in the chert-carbonate matrix ***(Figures 10F–G)*** or needles over 100 µm in length ***(Figure 10H–I)***. In plane-polarised

light, these structures are dark brown, translucent, strongly pleochroic, and silver in reflected light.

4.5. Kerogen characteristics

Raman spectra associated with TiO_2 polymorphs ***(Figure 10E)*** show three distinct types of kerogen crystallinity. Kerogen with well-defined D1- and G- bands at 1340 and 1605 cm^{-1} respectively ***(Figure 10E, spectrum I)*** is the most common and is observed in many other structures in the McLeary Formation ***(Figures 5F, 6E, 7G, 8F, 9I)***. The second type of kerogen has a spectrum with lower signal-to-noise ratio and poorly-resolved D1- and G-bands at 1363 and 1570 cm^{-1} respectively, and is less common ***(Figure 10E, spectrum G)***. The third type of kerogen is rare, noisy and has a small and weak G-band, and a D1-band region occupied by several resolvable peaks at 1147, 1193, 1305, 1407, and 1571 cm^{-1} ***(Figure 10E, spectrum D)***. Spectra D and G are not suitable for the Raman geothermometer calibrated on the basis of prograde kerogen and graphitic carbons in metapelite. We note however, that the latter spectrum shares some similarity with some occurrences in the co-eval Biwabik Formation ***(Figure 7i in Papineau et al., 2017)***. It remains unclear whether this represents contamination, syngenetic biomass, or possible diamondoids ***(e.g. Filik et al., 2006)***. A selection of other spectra of kerogen from this study were modelled using Lorentz functions ***(Lahfid et al., 2010)*** to calculate metamorphic temperatures between 241 and 358 °C for the McLeary Formation ***(Table 3)***. The formulae from ***Lahfid et al. (2010)*** were selected to calculate metamorphic temperatures because they use all five band parameters. The calculated temperatures are consistent with the temperature ranges implied by the D1/G intensities. At these temperatures, organic microfossils can remain well-preserved ***(Bernard et al., 2007)***.

The McLeary stromatolitic dolomites have relatively low TOC between 0.06 and 0.31 wt%, with a $\delta^{13}C_{org}$ average of -26.4 ± 2.3 ‰ (1 s.d.) ***(Table 2)***. Sample ***BgMc11041*** (see ***Figure 8*** kerogen maps) has the highest %TOC and the most negative $\delta^{13}C_{org}$ (-29.4 ‰), whereas ***BgMc11035***, which has notable pyrite grains, has the lowest %TOC (0.07 %) and the heaviest $\delta^{13}C_{org}$ values (-22.9 ‰). The McLeary dolomite also has $\delta^{13}C_{carb\text{-}PDB}$ values between -0.5 and 0.0 ‰, whereas the $\delta^{18}O_{carb\text{-}SMOW}$ values are between +19.5 and +23.5 ‰. Those $\delta^{13}C_{carb\text{-}PDB}$ values are comparable to those obtained by ***Hodgkiss et al. (2019)***; their values show a range between -1.5 and +1.0 ‰.

5. Discussion

5.1. Morphology of stromatolites

The morphology of stromatolites is partly controlled by environmental factors, allowing the reconstruction of depositional environments during stromatolite formation ***(Ricketts, 1979; Walter et al., 1992)***, however, it should also be noted that some morphotypes exist that are not specific to the depositional environment ***(Grey & Corkeron, 1998)***. In the McLeary Formation, stromatolites with decimetre-size domal morphologies ***(Figures 2A–D)*** are found in the Lower Zone of the Upper Member ***(Figure 1B)***, which according to ***Ricketts (1979)***, also contains ripples, partly eroded dessication cracks and herringbone cross-bedding. These features are indicative of a shallow-water environment with intense wave action, such as the intertidal zone ***(Ricketts, 1979)***. On the other hand, decimetre-size tabular bioherms with fragile millimetre-size bifurcate to multifurcate branching stromatolites ***(Figures 2E–F)*** are not found in association with rip-up structures or dessication cracks. Therefore, they likely formed in the low energy environment of a deeper intertidal zone with little wave action ***(Ricketts, 1979)***. These associations between stromatolite morphology and sedimentary

structures also support the conclusion drawn by ***Hofmann (1976)***, who stated that the microflora of the McLeary Formation inhabited intertidal mudflats and adjacent subtidal and supratidal environments. In this shallow-marine environment with thriving microbial communities, early diagenetic processes—both biotic and abiotic—would have been ubiquitous.

5.2. Sedimentology of McLeary stromatolites

The ubiquity of dolomitic carbonate ***(Figure 10B, Spectrum 5)*** is evidence of an environment that had a readily available source of Mg and favourable conditions for dolomite formation. Dolomite can be classed as microbially-induced or non-biological, however, for dolomite to precipitate from supersaturated solutions, kinetic barriers must be overcome ***(Land, 1998)***. In microbially-induced dolomite, these kinetic barriers are overcome due to methanogenesis and bacterial sulphate reduction (sulphate ions have an inhibiting effect on dolomite formation) ***(Baker & Kastner, 1981; Compton, 1988; Font et al., 2006)***. Additionally, EPS secreted by bacteria can have a kinetic effect promoting dolomite or proto-dolomite precipitation ***(Meister et al., 2013; Liu et al., 2020). Bontognali et al. (2010)*** also found that dolomite precipitation is initiated within EPS in microbial mats and the presence of charged clays can also help to trigger proto-dolomite formation ***(Liu et al., 2019b)***. The carboxyl groups produced when bacterial heterotrophs break down organic matter creates conditions that allow the nucleation of Mg-rich carbonates on their cell walls ***(Roberts et al., 2013; van Maldegem et al., 2019)***.

The alternations between carbonate, chert and organic matter in McLeary stromatolite laminae may support this link between biological processes and carbonate precipitation. Active microbial mats in the environment of the McLeary Formation produced

EPS, which helps to stabilise the mats against wave action ***(De Winder et al., 1999; Decho et al., 2005)***. The EPS also binds and concentrates Ca^{2+} and Mg^{2+} ions from the surrounding seawater, therefore when the EPS degrades, the alkalinity created by the released ions may additionally promote carbonate precipitation ***(Decho et al., 2005)***. Dolomite formation can also be influenced by the decay of cyanobacteria and experiments show that some cyanobacteria preferentially concentrate Mg as an organic complex ***(Greenfield, 1963; Gebelein and Hoffman, 1973)***. Hence, when cyanobacteria decay, Mg is released. Dolomite precipitation may also be induced by increased carbonate ion activity, due to an increase in alkalinity and/or dissolved inorganic carbon content ***(Meister et al., 2013)***. This demonstrates that changes in ocean alkalinity over time could strongly affect authigenic dolomite formation ***(Meister et al., 2013)***.

Non-biological dolomite can form via dissolution when pre-existing calcite is dissolved and then replaced by Mg-rich carbonate. During calcite dissolution, the Ca^{2+} produced combines with Mg^{2+} and CO_3^{2-} from the dolomitising fluid or Mg-rich clay ***(Weyl, 1959; Merino & Canals, 2011; Mehmood et al., 2018)***. In non-biological dolomite, the kinetic barriers to formation are overcome by negatively charged clays. Recent experiments have shown that dolomite precipitation under ambient conditions can be aided by the presence of clays such as illite and montmorillonite, with the latter being more effective at promoting precipitation due to its greater surface charge density ***(Liu et al., 2019b)***. Based on close relationship between microbial mat-like structures and dolomite, dolomite formation in the McLeary Formation appears to have been both microbially-induced and partly from the presence of EPS, but without abundant clays.

McLeary Formation stromatolites often show signs of complete or partial silicification ***(Figures 4A–B and 7A–B respectively)***. The chert in the samples can be divided into

546 microquartz and megaquartz (crystal sizes of <30 µm and 50–100 µm respectively) that
547 represent different stages of diagenesis ***(Knauth, 1994; Marin-Carbonne et al., 2014)***. Firstly,
548 an amorphous precursor precipitated from silica-rich fluid, then as diagenesis progressed to
549 the burial stage, this precursor crystallised into microquartz, and finally, once temperatures
550 surpassed 100 °C, the microquartz crystallised into megaquartz. Alternatively, microquartz can
551 also form via direct precipitation from seawater ***(Mackenzie and Gees, 1971)***. This direct
552 precipitation is plausible in the depositional environment of the McLeary Formation because
553 late Palaeoproterozoic oceans likely had higher concentrations of silica, since siliceous
554 organisms had not yet evolved ***(Maliva et al., 2005)***.
555 Chert granules similar to those in ***Figures 6A–B*** are also seen in the 1.878 Ga Gunflint
556 Formation in Canada ***(Marin-Carbonne et al., 2014)***. They are also similar to granules in the
557 Nastapoka GIF, although these granules have a rim of magnetite ***(Dodd et al., 2018)***. The silica
558 granules from the 3.47 Ga old Antarctic Creek Member of the Warrawoona Group, Western
559 Australia have dark rims of siderite and are composed of quartz chert. Although we did not
560 detect any siderite, the coarse-grained interiors are similar to the granules in ***Figures 6A–B***
561 ***(Stefurak et al., 2014)***. In contrast to the rounded McLeary Formation granules, those in the
562 2.63–2.45 Ga old Hamersley Group in Australia consist of ~100 µm, interlocking, polygonal
563 chert structures with white quartz rims. They also contain sedimentary layering which is
564 continuous across multiple granules, indicating that the granules are post-depositional
565 features ***(Rasmussen et al., 2015)***. However, because McLeary granules co-occur with sub-
566 rounded quartz clasts ***(Figure 6F)*** and their morphology does not resemble any patterns of the
567 BZ reaction (i.e. no concentric laminations nor radially-aligned blades), we suggest that both
568 wave-agitation and diagenesis played a role in the rounding of these granules. Some rounded,
569 single, early diagenetic quartz crystals contain fluid inclusions and microfossils ***(Figure 5A),***

akin to other observations of microfossils in granules from late Palaeoproterozoic chert ***(Walter et al., 1976; Knoll and Simonson, 1981; Papineau et al., 2017; Dodd et al., 2018)***. Hence, these rounded single quartz crystals are considered to be granules with an authigenic-diagenetic origin. Their formation could thus have involved direct biological influences as well as non-biological processes dependent on the presence of biomass.

Stylolites are a late diagenetic feature because they form as minerals and water are removed by dissolution pressure solution at burial depths of 0.1–1.0 km ***(Bathurst, 1980)***. The compaction that occurs during this stage of diagenesis causes carbonate minerals to dissolve, migrate via fluid flow, and precipitate elsewhere, leaving behind the largely siliciclastic minerals that are less soluble than the host rock ***(Moore, 1989; Koehn et al., 2016)***. In the McLeary Formation, rutile, anatase, feldspar, and oxide minerals were left behind during stylolite formation. Some of these minerals can be seen in sedimentological structures from stromatolites, which leads to the conclusion that these minerals or their precursors were present during diagenesis. Detrital TiO_2 was the likely source for the anatase and rutile that compose the needles ***(Figures 10F–I)***.

5.3. Microfossils and organic matter

The filamentous morphology of the microfossils in ***Figures 5A–D*** is identical to that of *Halythrix sp.*, previously described in black chert from the slightly older Kasegalik Formation by ***Hofmann (1976, Plate 1, Figures 18–19)***, but not yet reported in the McLeary Formation. The examples described by ***Hofmann (1976)*** consist of filaments that are, on average, 2.4–2.9 µm wide and at least 70–80 µm long. While the filaments are smaller in diameter and longer in the Kasegalik Formation than the McLeary microfossils documented in this study, their segmented and curved morphologies are remarkably similar. The curves of these microfossils

are clearly shown in ***Figure 5A*** and may be due to the fact that *Halythrix sp.* does not possess an enclosing sheath, so there is less connectivity between cells ***(Boal & Ng, 2010)***. *Halythrix nodosa* has previously been found in the 896 ± 24 Ma Bitter Springs Group in central Australia, and consists of 4.5 µm wide and 4.2 µm long spool-shaped cells arranged into 25–30 µm long filaments ***(Schopf, 1968)***. The latter have a similar size to the cells in ***Figures 5A–D,*** but the Bitter Springs Group cells are less elongate. Similar 1000 µm long microbial filaments were reported by ***Schopf et al. (2015)*** in black chert from the ~2.0 Ga old Duck Creek Formation in Western Australia. These filaments can be divided into three classes: 7-9 µm wide filaments with elongate cells, 1–4 µm wide filaments with bead-shaped cells, and threadlike filaments with a diameter of ≤1 µm. The almost contemporaneous 1.878 Ga old Gunflint Formation in Ontario, Canada has pyritised and kerogenous *Gunflintia* ***(Wacey et al., 2013; Papineau et al., 2017)***. These microfossils consist of segmented filaments but, unlike the filaments in the McLeary Formation, they have an enclosing sheath and are therefore less sinuous ***(Boal & Ng, 2010; Wacey et al., 2013)***.

The filaments in this study are preserved by partial pyritisation which is reflected in the fact that Raman spectra show a mixture of pyrite and kerogen ***(Figure 5F)***. Despite the rarity of pyritised soft-bodied organisms ***(Wacey et al., 2013)***, the stromatolite microenvironment provides suitable conditions for microbially-mediated pyritisation, thus preserving basic microbial morphology ***(Noffke et al., 2013)***. During early diagenesis, bacteria use dissolved sulphate to oxidise organic matter, leading to the production of bicarbonate and hydrogen sulphide ***(Berner, 1971; Gluyas, 1984)***. The hydrogen sulphide produced can react with dissolved or solid iron to form pyrite ***(Raiswell & Plant, 1980)***, such that intense anaerobic decay by sulphate-reducing bacteria can lead to pyritisation ***(Wacey et al., 2013)***. As diagenesis proceeds, the produced bicarbonate can react with dissolved Ca^{2+}, as well as

618 Mg^{2+} and Fe^{2+}, to form micritic carbonate minerals. The coiled filament in ***Figure 5K*** shares
619 morphological similarity with the more tighly coiled microfossil *Obruchevela* (λ ~ 2μm) and
620 *Heliconema* (λ ~ 10μm), both found inside apatite granules in the Ediacaran Doushantuo
621 Formation ***(She et al., 2014)***. The McLeary coiled filament also differs from other coiled
622 filamentous microfossils by being preserved in a halo of clearer chert, which is possibly a
623 diagenetic feature related to the taphonomy of EPS in stromatolite layers rich in biomass.

624 The kerogen-rich degraded coccoid-like structures in ***Figures 7E–F*** are similar to those
625 formed by coccoidal microfossils ***(Hofmann, 1975)***, but their relatively poor level of
626 preservation makes any specific taxonomic assignment ambiguous. Nevertheless, they do
627 resemble *Sphaerophycus parvum* previously described in the chert of the McLeary and
628 Kasegalik Formations ***(Hofmann, 1976, Plate 3, Figures 1–6)***, and they are also
629 morphologically indistinguishable from the Bitter Springs occurrences. *Sphaerophycus parvum*
630 is 1.5–3.5 μm in diameter and often forms irregular-shaped clusters. Like the kerogen-rich
631 coccoid-like structures in ***Figures 7E–F***, *Sphaerophycus parvum* cells also have a dark interior,
632 which is thought to be the result of water loss during decay ***(Hofmann, 1975)***. The presence
633 of these silicified microfossils suggests that silica precipitation occurred close to the sediment-
634 water interface in peritidal carbonates ***(Simonson, 1985; Maliva et al., 2005)***, and the colour
635 gradient suggests that they were preserved partway through the decay process ***(Hofmann,***
636 ***1975)***.

637 The TOC and $\delta^{13}C$ of the McLeary Formation stromatolites were analysed to detect
638 possible molecular signatures. Bulk geochemical analyses show low TOC values that resemble
639 low abundances of kerogen. The stable carbon isotope compositions of the kerogen with an
640 average $\delta^{13}C_{org}$ of -26.4 ‰ and a similar average $\Delta\delta^{13}C_{org\text{-}carb}$ value of -26.2 ‰ for the isotopic
641 fractionation between bulk organic and carbonate carbon, are indicative of photoautotrophic

carbon fixation in this environment ***(e.g. Schidlowski, 2001)***. Additionally, the corresponding carbonates ($\delta^{13}C_{carb}$ -0.5 and 0.0 ‰) show no evidence of the Lomagundi-Jatuli Event. Instead, these $\delta^{13}C$ values fall in the range of other late Palaeoproterozoic successions in the aftermath of the Lomagundi-Jatuli Event ***(e.g. Karhu and Holland, 1996)***. Collectively, low contents of organic matter in stromatolitic dolomite and typical $\delta^{13}C$ values for both organic matter and carbonate indicate a microbial ecosystem with nearly-balanced oxygenic photosynthesis and heterotrophic recycling of carbon.

5.4. Oxidation of biomass during diagenesis

Fluid inclusions in quartz crystals ***(Figure 5A–E)*** include a mixture of CO_2 and CH_4. They are found alongside *Halythrix sp.* microfossils, which suggests that these gases could have formed during the late diagenetic to thermal degradation of biochemical macromolecules from biomass, releasing CO_2 and CH_4. However, in the absence of $\delta^{13}C$ values for this CH_4, its provenance remains unclear ***(Vandenbroucke & Largeau, 2007)***. Along with the co-occurrence of partly pyritised *Halythrix sp.* microfossils, these fluid inclusions imply that this single quartz crystal is authigenic, granule-like, and that it grew throughout diagenesis. Hence, such outsized and sub-angular crystals are not necessarily detrital, and we discount the possibility that it could be from weathered Kasegalik clasts on the basis of the intergrown nature of the grain edge, the excellent preservation of its microfossils and fluid inclusions, and the chemical precipitate and biological nature of the McLeary depositional environment. The carbonate rhomb in ***Figure 8G–H*** also bears a striking resemblance to those reported by ***Papineau et al. (2017)*** from the Gunflint Formation. They both have a similar size (less than 500 µm wide) as well as a darker core and small particles of kerogen along the edge. These

665 rhombs are concentrically-zoned with kerogen, which is an indication of diagenetic carbonate
666 produced from the oxidation of biomass ***(Papineau et al., 2017)***.

667 Some chert granules possess a dark, organic-rich rim ***(Figures 6A–B)***. This has also been
668 reported for chert granules from the 3.5–3.2 Ga old Barberton Greenstone Belt in South Africa,
669 where the rims contain a carbonaceous biofilm coating ***(Trower & Lowe, 2016)***. Similar
670 structures have also been reported in the contemporaneous Sokoman Iron Formation in
671 Québec by ***Knoll and Simonson (1981)***, as well as in the Gunflint Formation in Ontario, where
672 they tend to have concentric laminations of organic matter and microscopic euhedral
673 dolomite inclusions ***(Papineau et al., 2017)***. In particular, the different degree of crystallinity
674 based on Raman spectra of microscopic particles of kerogen in diagenetic features of the
675 McLeary Formation ***(Figure 10E, Table 3)*** is consistent with variable levels of functional groups
676 and thus with the variable oxidation or heterogeneous mixtures (such as protein- or EPS-rich)
677 of biomass during diagenesis. For instance, during the diagenesis and low-temperature
678 metamorphism of banded iron formations, biomass progressively converts to kerogen, apatite
679 and carbonate ***(Dodd et al., 2019)***. These authigenic minerals are key because they tend to
680 remain associated with kerogen and graphitic carbon, and these types of graphitic carbons
681 can be constituted by more than one type of crystallinity ***(Dodd et al., 2019; Papineau et al.,***
682 ***2019)***.

683 The needle-like crystals of rutile are interpreted as authigenic because they show no
684 signs of erosion due to transport, and hyperspectral images show that they are intergrown
685 with the carbonate matrix ***(Figures 10G, 10I)***. Rutile needles of this size can form during low-
686 grade metamorphism (greenschist and amphibolite facies) ***(Banfield & Veblen, 1991)***. Based
687 on the chlorite, sphene, sericite, prehnite and pumpellyite mineral assemblage observed in
688 the McLeary Formation ***(Leggett, 1974; Stirbys, 1975; and Ricketts, 1979)***, and the low degree

689 of crystallinity of kerogen that indicates crystallisation temperatures between about 241 and
690 358 °C ***(Table 3)***, the metamorphic facies of the McLeary Formation is most consistent with
691 the prehnite-pumpellyite to lower greenschist facies. According to ***Morad (1986)***, it is also
692 possible for rutile to precipitate from Ti-rich pore fluids where the source of Ti is the
693 dissolution of other Ti-bearing detrital or hydrothermal minerals such as brookite (the
694 orthorhombic polymorph of TiO_2) ***(Force, 1991)***. In the McLeary Formation, such fluid-
695 deposition is supported by the common association of rutile needles with anatase and alkali
696 feldspar, which may have formed authigenically from alkaline solutions and detrital clays such
697 as illite.

698 Biology likely modulates the concentration and formation of TiO_2 crystals because
699 association between organic matter and TiO_2 polymorphs has been described before in both
700 Precambrian and younger rocks. ***Foucher et al. (2016)*** reported that carbon is frequently
701 associated with anatase in 3.446 Ga old Kitty's Gap chert from Pilbara, Australia. Also bitumen
702 is closely associated with anatase in Cambrian shales from the Zhajin section in the Yangtze
703 platform, South China ***(Liu et al., 2014)***, in Archaean shales and siltstones of the
704 Witwatersrand Supergroup in South Africa ***(Fuchs et al., 2015)***, and in other petroleum-
705 bearing sedimentary basins where the alteration of organic matter leads to a decrease in pH
706 ***(Helgeson et al., 1993)***. Lipids have been found within bacteriomorphic rods permineralised
707 by anatase in the 35.3 Ma old Chesapeake Bay impact structure in Virginia, USA ***(Glamoclija***
708 ***et al., 2009)***, and grains of anatase also occur along the edges of the filamentous microfossil
709 *Eoleptonema apex* from the ~3.46 Ga old Apex chert ***(Bower et al., 2016)***.

710 Furthermore, when methanogenesis occurs during diagenesis, organic compounds
711 such as acetic and oxalic acids are produced, leading to a decrease in the pH of pore fluids.
712 This is important because the dissolution and precipitation of Ti-bearing detrital nano-crystals

713 is favored at lower pH, and if the pH subsequently increases and the ionic strength decreases,
714 nano-crystals can grow to larger sizes ***(Schulz et al., 2016)***. Thus the larger acicular structures
715 with TiO_2 in the McLeary Formation may be the product of low-grade metamorphism of
716 diagenetic minerals associated with organic matter from biomass.

717 It should also be noted that apatite can form during the degradation of microbial
718 biomass and remains preferentially associated with organic matter, even through to
719 greenschist and amphibolite facies metamorphism ***(Papineau et al., 2016; 2017; 2019)***.
720 Therefore, the occasional microscopic grains of fluorapatite in kerogen-rich stromatolite
721 laminae ***(Figures 7C–D)*** are most consistent with an origin from decayed biomass. This
722 association between stromatolite laminae and fluorapatite could also have been aided by the
723 photocatalytic properties of TiO_2 on the oxidation of organic matter ***(e.g. Fujishima & Zhang,***
724 ***2005)***.

725 The euhedral habit and general lack of oxidative weathering on most pyrite crystals
726 suggest that it has an authigenic origin. Diagenetic pyrite is formed via a reaction between
727 dissolved iron and hydrogen sulphide ***(Raiswell & Plant, 1980)***, with the latter mediated by
728 microbial sulphate reduction and thus microbial oxidation of biomass.

729 Framboids form in weakly reducing conditions near the sulphidic zone in anoxic
730 sediments during diagenesis ***(Raiswell & Berner, 1985)*** and since these reactions need
731 partially oxidised sulphur, they are usually restricted to redox boundaries ***(Canfield &***
732 ***Thamdrup, 1994)***. It should be noted that the framboid in ***Figure 9C*** is more euhedral and
733 considerably larger than what is typical for pyrite framboids. For example, those reported by
734 ***She et al. (2016)*** in the Neoproterozoic Doushantuo Formation are ~5 μm in diameter, and
735 consist of nanometre-size pyrite crystals arranged into a roughly spherical shape. These

differences may be explained by a higher degree of recrystallisation within the McLeary Formation that experienced higher temperatures and repeated metamorphism.

5.5. Comparison with patterns in chemically oscillating reactions

Below are two possible and relevant equations for the BZ reaction with bromate and sulphate as example oxidisers for illustrative purposes:

$$3CH_2(COOH)_2 + 4BrO_3^- \rightarrow 4Br^- + 9CO_2 + 6H_2O \quad (1)$$

$$CH_2(COOH)_2 + H_2SO_4 \rightarrow 3CO_2 + H_2S + 2H_2O \quad (2)$$

When the redox-sensitive dye ferroin (phenanthroline ferrous sulphate) is used, the reaction becomes auto-catalytic, and micrometre-to-decimetre scale circularly-concentric and equidistant chemical waves propagate radially from an epicentre, forming patterns similar to the circularly-concentric and radially-alligned mineral patterns in diagenetic spheroids ***(Papineau et al., 2017; Papineau, 2020)***.

The patterns that are formed by the above reactions share close similarity to several morphological features in the McLeary Formation stromatolite samples (see also ***Figure 1 in Papineau, 2020***):

- Circularly-concentric and equidistant laminations around oxidation spots that span sub-millimetre sizes, compared to submillimetre to decimetre sizes in experiments
- Cavity-shaped structures formed from the destructive interference of circular chemical waves
- Parallel-layered and wavy patterns, including stromatolite-like, columnar-turbinate laminated pattern
- Colour gradients in laminations

- Globular texture with three-dimensional grape-like morphology

In detail, the oriented chert crystals that fill cavity-like structures in stromatolites ***(Figures 8A–E)*** are morphologically similar to 'cavity' patterns seen in BZ experiments ***(Papineau et al., 2017; Papineau, 2020)***. Firstly, many small clusters of possible degraded coccoidal microfossils composed of diffuse kerogen occur in the geometric epicentres of these diagenetic spheroids, along with rutile and micron-size carbonate ***(Figures 8A–E)***. The association of microfossils with concentrically-layered and equidistant laminations of chert-carbonate structures was recently reported from late Palaeoproterozoic granular chert from the Lake Superior area ***(Papineau et al., 2017)*** and worldwide late Palaeoproterozoic granular iron formations ***(Dodd et al., 2018).*** The example in ***Figures 8A–B*** shows two sets of laminations from two different origins combining to create a pattern of destructively interfered circular waves with a series of apex corners between two colonies of microbes. These coccoid-like structures are composed of kerogen, and since they are located at the epicentre of the kerogen-rich laminations (i.e. the source of the chemically oscillating reactions), these processes could have contributed to the decarboxylation of the biomass and the formation of these quartz structures during diagenesis.

In carbonate rosettes ***(Figures 8I–J)***, a three-dimensional, globular morphology can be seen when the focus on the optical microscope is changed, and they display a colour gradient that is a reflection of their kerogen content. These two BZ morphological traits—combined with kerogen in their epicentre that once contained organic acids—suggest that these rosettes were produced by chemically oscillating reactions. In addition, pyrite concretions occur in decimetre-size columnar stromatolites ***(Figures 3D and 9A),*** and they contain rounded-shaped concretionary pyrite clusters and framboids ***(Figure 9B)***, which are in turn composed of euhedral to subhedral pyrite crystals ***(Figure 9C)***. We suggest that such microscopic diagenetic

spheroids inside a centimetric concretion is an analogous pattern to some of those produced by chemically oscillating reactions. These are circularly-concentric and expand radially outward with sizes that span between about one hundred microns to decimetre scales ***(Papineau, 2020)***. This kind of non-biological, out-of-equilibrium, and spontaneous reaction thus provides an elegant explanation for the commonly concentric and radial geometries of these structures.

A proposed sequence of events is as follows. Hydrogen sulphide produced by the bacterial oxidation of organic matter during early diagenesis first reacts with iron to form pyrite concretions, isolated euhedral pyrite crystals, and framboids ***(Figures 3B–D, 9)***. This process also causes the pyritisation of some microfossils ***(Figures 5A–D)***. Isopachous quartz ***(Figures 4I–J, 8C–E)*** then forms and becomes overgrown by botryoids produced by chemically oscillating reactions. The latter is illustrated in ***Figure 8E*** where the Raman image shows kerogen laminations that overprint quartz. The other McLeary spheroids probably also form at this point ***(Figures 8G–H)***. During the burial stage of diagenesis, the formation of chert lenses cut across various textures, such as isopachous quartz and patterns produced by chemically oscillating reactions ***(Figures 4I–J)***. At this stage, increasing pressure due to burial leads to dissolution, mobilisation of pore fluids, and carbonate release from compaction and precipitated as sparry crystals ***(Figures 4G–H)***. During late burial diagenesis, stylolitisation occurs ***(Figures 3C, 9E–H) (Moore, 1989)***. Finally, the whole rock sequence is then subjected to low-grade regional metamorphism.

There are a few possible sources for compounds needed for chemically oscillating reactions in the environment. In the classical BZ reaction, phenanthroline ferrous sulphate is used as a catalyst for the cyclic reactions between a strong oxidiser, its halide salt, sulphuric acid, and malonic acid ***(Zaikin & Zhabotinsky, 1970)***. A higher concentration of sulphate is

807 thought to have been present in the ocean elsewhere around the Superior Craton during the
808 deposition of the McLeary Formation, where oxidative terrestrial weathering after the GOE
809 must have delivered sulphate, as well as phosphate to shallow oceans ***(Cameron, 1983;***
810 ***Canfield, 1998; Papineau et al., 2005; 2007)***. A likely source of organic acid reactants for
811 chemically oscillating reactions can be derived from biomass, which was stimulated by
812 increased phosphate delivery during and after the GOE ***(Papineau, 2010)***. The concentration
813 of other reactants such as strong oxidants (including bromate, iodate, and hydrogen peroxide
814 that can all produce BZ patterns ***(Briggs & Rauscher, 1973)***), was also increased after the GOE,
815 as inferred from the higher iodine concentration in Palaeoproterozoic carbonates ***(Hardisty et***
816 ***al., 2014; 2017; Wei et al., 2019)***. In fact, ***Hardisty et al. (2017)*** found that there was an
817 increased level of iodine in Neo- and Palaeoproterozoic carbonate compared to Archaean
818 carbonates. These authors inferred that increased environmental iodate availability may have
819 been initiated by the oxygenation of surface-waters. Another potential oxidiser present then
820 is bromate because many marine cyanobacteria produce a range of organobromine
821 compounds ***(Gribble, 1999; 2000)***. Such compounds could have been released during the
822 decomposition of coccoidal cyanobacteria, the possible precursors to the kerogen-rich
823 spheres in ***Figures 8A–E***, and this could possibly have contributed to cause spontaneous
824 chemically oscillating reactions and produce circularly-concentric and radial patterns.
825

826 ## 6. Conclusions

827 Various diagenetic structures and mineral assemblages are preserved in two
828 morphological types of stromatolitic dolomite from the late Palaeoproterozoic McLeary
829 Formation. Most of the original organic carbon in these stromatolites has been lost through
830 biological respiration and non-biological diagenetic oxidation. Disordered organic matter in

these stromatolites is consistent with peak metamorphic temperatures between 241 and 358 ^{o}C. Diagenetic structures include black chert and pyrite concretions, microfossiliferous quartz and chert granules, carbonate rosettes and pyrite framboids (or rosettes), isopachous quartz with circularly-concentric laminations of kerogen which have patterns of destructively interfered chemical waves and surround microfossils. Within these structures there are accessory minerals such as rutile, anatase, pyrite, apatite, feldspar, possible clay, and three types of organic matter. Extensive diagenetic processes were operating during the decomposition of biomass in the McLeary Formation, which were facilitated jointly by the presence of microbial communities and chemically oscillating reactions.

The role of microbial activity in diagenesis was promoted by oxic conditions, a higher concentration of sulphate in the oceans, and large amounts of organic matter available for oxidation during diagenesis. Filamentous microfossils are preserved in granules of coarse quartz, the result of the partial replacement of organic matter by pyrite. The close association of these *Halythrix sp.* filaments with CO_2, CH_4 and fluid inclusions suggests the C-compounds originated from the cracking of biomass during diagenesis or metamorphism. We therefore infer that such inclusions in these metamorphosed sedimentary rocks can be biosignatures. The organic matter in McLeary stromatolites is primarily in the form of kerogen and tends to be associated with microbial and stromatolite laminations, but also with abiotic diagenetic structures, and with minerals such as quartz, dolomite, pyrite, apatite, and TiO_2 polymorphs.

The new observations for the late Palaeoproterozoic dolomitic stromatolites from the McLeary Formation suggest that these microbial environments were sites for the diagenetic decomposition of organic matter. Chemically oscillating reactions are suggested to also have taken place in the McLeary Formation, as they have been suggested to participate in the formation of diagenetic spheroids in the co-eval southern Superior margin ***(Papineau et al.,***

855 ***2017)***, at a time of increased environmental oxygenation. The morphology and composition
856 of chert granules, carbonate rosettes, pyrite framboids and concretions, and zoned dolospar
857 are partly consistent with the products of chemically oscillating reactions, however there is no
858 associated ^{13}C-depleted carbonate in the McLeary Formation, as has been reported from the
859 southern Superior margin. This new model is plausible because the reactants necessary for
860 chemically oscillating reactions have been argued to have been more abundant in this post-
861 GOE environment. We conclude that a combination of factors was instrumental in producing
862 diagenetic structures in the McLeary stromatolitic dolomite, including increased carboxylic
863 acids from primary producers, higher sulphate from increased continental weathering, and
864 high iodate in carbonates.
865

866 ## 7. Acknowledgements

867 We thank W. Bleeker, P. Strother, C. Hallmann, and C. Swarth for help in the field and
868 useful discussions as well as V. Thiel for discussion. DP and MF thank the NASA Astrobiology
869 Institute (grant # NNA04CC09A), the W.H. Keck Foundation (Grant 2007-6-29), and Carnegie
870 of Canada for funding field work in the Nastapoka and Belcher Groups of Canada. The crews
871 of S/V Kakivaq and Arctic Kingdom Polar Expeditions are thanked for logistical support in the
872 Hudson Bay. The Nunavut Research Institute, Qikiqtani Inuit Association, and CLEY are
873 thanked for permits allowing our scientific research on Inuit-owned lands. ZS and DP also
874 acknowledge financial support from the Strategic Priority Research Program of Chinese
875 Academy of Sciences (grant# XDB26020102) and the National Natural Science Foundation of
876 China (grant # 41272038). For isotope analyses, we thank Y. Lin, University of California
877 Riverside. We would also like to thank the editor Frances Westall and the anonymous
878 reviewers for providing constructive feedback.

8. References

Akin, S. J., Pufahl, P. K., Hiatt, E. E., & Pirajno, F. (2013). Oxygenation of shallow marine environments and chemical sedimentation in Palaeoproterozoic peritidal settings: Frere Formation, Western Australia. Sedimentology, 60(7), 1559–1582.

Allwood, A. C., Rosing, M. T., Flannery, D. T., Hurowitz, J. A., & Heirwegh, C. M. (2018). Reassessing evidence of life in 3,700-million-year-old rocks of Greenland. Nature, 563(7730), 241–252.

Arndt, N. T., & Todt, W. (1994). Formation of 1.9-Ga-old Trans-Hudson continental crust: Pb isotopic data. Chemical Geology, 118(1-4), 9–26.

Baker, P. A., & Kastner, M. (1981). Constraints on the formation of sedimentary dolomite. Science, 213(4504), 214–216.

Banfield J. F., & Veblen, D. R. (1991). The structure and origin of Fe-bearing platelets in metamorphic rutile. American Mineralogist, 76(1-2), 113–127.

Bathurst, R. G. (1980). Lithification of carbonate sediments. Science Progress (1933–), 451–471.

Bernard, S., Benzerara, K., Beyssac, O., Menguy, N., Guyot, F., Brown Jr, G. E., & Goffé, B. (2007). Exceptional preservation of fossil plant spores in high-pressure metamorphic rocks. Earth and Planetary Science Letters, 262(1–2), 257–272.

Berner, R. A. (1971). Principles of Chemical Sedimentology (1st Ed). McGraw Hill.

Bleeker, W. (2003). The late Archean record: a puzzle in ca. 35 pieces. Lithos, 71(2–4), 99–134.

Boal, D., & Ng, R. (2010). Shape analysis of filamentous Precambrian microfossils and modern cyanobacteria. Paleobiology, 36(4), 555–572.

902 Bontognali, T. R., Vasconcelos, C., Warthmann, R. J., Bernasconi, S. M., Dupraz, C.,
903 Strohmenger, C. J., & McKenzie, J. A. (2010). Dolomite formation within microbial mats
904 in the coastal sabkha of Abu Dhabi (United Arab Emirates). Sedimentology, 57(3), 824–
905 844.
906 Bosak, T., Bush, J. W. M., Flynn, M. R., Liang, B., Ono, S., Petroff, A. P., & Sim, M. S. (2010).
907 Formation and stability of oxygen-rich bubbles that shape photosynthetic mats.
908 Geobiology, 8(1), 45–55.
909 Bosak, T., Knoll, A. H., & Petroff, A. P. (2013). The meaning of stromatolites. Annual Review of
910 Earth and Planetary Sciences, 41, 21–44.
911 Bower, D. M., Steele, A., Fries, M. D., Green, O. R., & Lindsay, J. F. (2016). Raman imaging
912 spectroscopy of a putative microfossil from the ~3.46 Ga Apex chert: Insights from
913 quartz grain orientation. Astrobiology, 16(2), 169–180.
914 Brehm, U., Krumbein, W. E., & Palińska, K. A. (2003). Microbial spheres: a novel
915 cyanobacterial–diatom symbiosis. Naturwissenschaften, 90(3), 136–140.
916 Briggs, T. S., & Rauscher, W.C. (1973). An oscillating iodine clock. Journal of Chemical
917 Education, 50(7), 496.
918 Byerly, G. R., Lower, D. R. and Walsh, M. M. (1986). Stromatolites from the 3,300–3,500-Myr
919 Swaziland Supergroup, Barberton Mountain Land, South Africa. Nature, 319(6053),
920 489–491.
921 Cameron, E. M. (1983). Evidence from early Proterozoic anhydrite for sulphur isotopic
922 partitioning in Precambrian oceans. Nature, 304(5921), 54–56.
923 Canfield, D. E. (1998). A new model for Proterozoic ocean chemistry. Nature, 396(6710), 450–
924 453.

925 Canfield, D. E. (2005). The early history of atmospheric oxygen: homage to Robert M. Garrels.
926 Annual Review of Earth and Planetary Sciences, 33, 1–36.
927 Canfield, D. E., & Thamdrup, B. (1994). The production of 34S-depleted sulfide during bacterial
928 disproportionation of elemental sulfur. Science, 266(5193), 1973–1975.
929 Compton, J. S. (1988). Degree of supersaturation and precipitation of organogenic dolomite.
930 Geology, 16(4), 318–321.
931 De Winder, B., Staats, N., Stal, L. J., & Paterson, D. M. (1999). Carbohydrate secretion by
932 phototrophic communities in tidal sediments. Journal of Sea Research, 42(2), 131–146.
933 Decho, A. W., Visscher, P. T., & Reid, R. P. (2005). Production and Cycling of Natural Microbial
934 Exopolymers (EPS) within a Marine Stromatolite. Palaeogeography, Palaeoclimatology,
935 Palaeoecology, 219(1), 71–86.
936 Dimroth, E., Baragar, W. R. A., Bergeron, R., & Jackson, G. D. (1970). The Filling of the Circum-
937 Ungava Geosyncline. Symposium on Basins and Geosynclines of the Canadian Shield,
938 Geological Survey of Canada Paper, 70–40.
939 Djokic, T., van Kranendonk, M. J., Campbell, K. A., Walter, M. R., & Ward, C. R. (2017). Earliest
940 signs of life on land preserved in ca. 3.5 Ga hot spring deposits. Nature
941 Communications, 8, 15263.
942 Dodd, M. S., Papineau, D., She, Z. B., Manikyamba, C., Wan, Y. S., O'Neil, J., Karhu, J. A., Rizo,
943 H., & Pirajno, F. (2019). Widespread occurrences of variably crystalline 13C-depleted
944 graphitic carbon in banded iron formations. Earth and Planetary Science Letters, 512,
945 163–174.
946 Dodd, M. S., Papineau, D., She, Z., Fogel, M. L., Nederbragt, S., & Pirajno, F. (2018). Organic
947 remains in late Palaeoproterozoic granular iron formations and implications for the
948 origin of granules. Precambrian Research, 310, 133–152.

949 Filik, J., Harvey, J. N., Allan, N. L., May, P. W., Dahl, J. E., Liu, S., & Carlson, R. M. (2006). Raman
950 spectroscopy of diamondoids. Spectrochimica Acta Part A: Molecular and
951 Biomolecular Spectroscopy, 64(3), 681–692.
952 Flannery, D. T., Allwood, A. C., Hodyss, R., Summons, R. E., Tuite, M., Walter, M. R., & Williford,
953 K. H. (2019). Microbially influenced formation of Neoarchean ooids. Geobiology, 17(2),
954 151-160.
955 Font, E., Nédélec, A., Trindade, R. I. F., Macouin, M., & Charrière, A. (2006). Chemostratigraphy
956 of the Neoproterozoic Mirassol d'Oeste cap dolostones (Mato Grosso, Brazil): an
957 alternative model for Marinoan cap dolostone formation. Earth and Planetary Science
958 Letters, 250(1–2), 89–103.
959 Force, E. R. (1991). Geology of titanium-mineral deposits (Vol. 259). Geological Society of
960 America.
961 Foucher, F., Westall, F., Brandstätter, F., Demets, R., Parnell, J., Cockell, C. S., Edwards, H. G.,
962 Bény, J. M., & Brack, A. (2010). Testing the survival of microfossils in artificial martian
963 sedimentary meteorites during entry into Earth's atmosphere: the STONE 6
964 experiment. Icarus, 207(2), 616–630.
965 Frantz, C. M., Petryshyn, V. A., & Corsetti, F. A. (2015). Grain trapping by filamentous
966 cyanobacterial and algal mats: implications for stromatolite microfabrics through time.
967 Geobiology, 13(5), 409–423.
968 Fuchs, S., Schumann, D., Williams-Jones, A. E., & Vali, H. (2015). The growth and concentration
969 of uranium and titanium minerals in hydrocarbons of the Carbon Leader Reef,
970 Witwatersrand Supergroup, South Africa. Chemical Geology, 393, 55–66.
971 Fujishima, A., & Zhang, X. (2005) Titanium dioxide photocatalysis: present situation and future
972 approaches. Comptes Rendus de Chimie 8, 750–760.

973 Gebelein, C. D., & Hoffman, P. (1973). Algal origin of dolomite laminations in stromatolitic
974 limestone. Journal of Sedimentary Research, 43(3), 603–613.
975 Glamoclija, M., Steele, A., Fries, M., Schieber, J., Voytek, M. A., & Cockell, C. S. (2009).
976 Association of anatase (TiO_2) and microbes: Unusual fossilization effect or a potential
977 biosignature?. Special Paper of the Geological Society of America, 458, 965–975.
978 Gluyas, J. G. (1984). Early carbonate diagenesis within Phanerozoic shales and sandstones of
979 the NW European shelf. Clay Minerals, 19(3), 309–321.
980 Greenfield, L. J. (1963). Metabolism and concentration of calcium and magnesium and
981 precipitation of calcium carbonate by a marine bacterium. Annals of the New York
982 Academy of Sciences, 109(1), 23–45.
983 Grey, K., & Corkeron, M. (1998). Late Neoproterozoic stromatolites in glacigenic successions
984 of the Kimberley region, Western Australia: evidence for a younger Marinoan
985 glaciation. Precambrian Research, 92(1), 65–87.
986 Gribble, G. W. (1999). The diversity of naturally occurring organobromine compounds.
987 Chemical Society Reviews, 28(5), 335–346.
988 Gribble, G. W. (2000). The natural production of organobromine compounds. Environmental
989 Science and Pollution Research, 7(1), 37–49.
990 Hamilton, M., Buchan, K. L., Ernst, R. E., & Scott, G. M. (2009). Widespread and Short-Lived
991 1870 Ma Mafic Magmatism along the Northern Superior Craton Margin. American
992 Geophysical Union-Geological Association of Canada, Joint Meeting (abstract# GA11A-
993 01).
994 Hardisty, D. S., Lu, Z., Bekker, A., Diamond, C. W., Gill, B. C., Jiang, G., Kah, L. C., Knoll, A. H.,
995 Loyd, S. J., Osburn, M. R., & Planavsky, N. J. (2017). Perspectives on Proterozoic surface

ocean redox from iodine contents in ancient and recent carbonate. Earth and Planetary Science Letters, 463, pp.159–170.

Hardisty, D. S., Lu, Z., Planavsky, N. J., Bekker, A., Philippot, P., Zhou, X., & Lyons, T. W. (2014). An iodine record of Paleoproterozoic surface ocean oxygenation. Geology, 42(7), 619–622.

Helgeson, H. C., Knox, A. M., Owens, C. E., & Shock, E. L. (1993). Petroleum, oil field waters, and authigenic mineral assemblages Are they in metastable equilibrium in hydrocarbon reservoirs. Geochimica et Cosmochimica Acta, 57(14), 3295–3339.

Hickman-Lewis, K., Gautret, P., Arbaret, L., Sorieul, S., De Wit, R., Foucher, F., Cavalazzi B, & Westall, F. (2019). Mechanistic morphogenesis of organo-sedimentary structures growing under geochemically stressed conditions: keystone to proving the biogenicity of some Archaean stromatolites? Geosciences, 9(8), 359.

Hodgskiss, M. S., Dagnaud, O. M., Frost, J. L., Halverson, G. P., Schmitz, M. D., Swanson-Hysell, N. L., & Sperling, E. A. (2019). New insights on the Orosirian carbon cycle, early Cyanobacteria, and the assembly of Laurentia from the Paleoproterozoic Belcher Group. Earth and Planetary Science Letters, 520, 141–152.

Hofmann, H. J. (1975). Stratiform Precambrian stromatolites, Belcher Islands, Canada; relations between silicified microfossils and microstructure. American Journal of Science, 275(10), 1121–1132.

Hofmann, H. J. (1976). Precambrian microflora, Belcher Islands, Canada: significance and systematics. Journal of Paleontology, 1040–1073.

Homann, M. (2019). Earliest life on Earth: Evidence from the Barberton Greenstone Belt, South Africa. Earth-Science Reviews, 196, 102888.

1019 Karhu, J. A., & Holland, H. D. (1996). Carbon isotopes and the rise of atmospheric oxygen.
1020 Geology, 24(10), 867–870.
1021 Knauth, L.P. (1994). Petrogenesis of chert. In P. J. P. Heaney, C. T. Prewitt & G. V. Gibbs (Eds.),
1022 Silica: Physical Behavior, Geochemistry and Materials Applications (pp. 233–258).
1023 Mineralogical Society of America.
1024 Knoll, A. H., & Simonson, B. (1981). Early Proterozoic microfossils and penecontemporaneous
1025 quartz cementation in the Sokoman Iron Formation, Canada. Science, 211(4481), 478–
1026 480.
1027 Koehn, D., Rood, M. P., Beaudoin, N., Chung, P., Bons, P. D., & Gomez-Rivas, E. (2016). A new
1028 stylolite classification scheme to estimate compaction and local permeability
1029 variations. Sedimentary Geology, 346, 60–71.
1030 Kouketsu, Y., Mizukami, T., Mori, H., Endo, S., Aoya, M., Hara, H., Nakamura, D., & Wallis, S.,
1031 2014. A new approach to develop the raman carbonaceous material geothermometer
1032 for low-grade metamorphism using peak width. Island Arc, 23(1), 33–50.
1033 Lahfid, A., Beyssac, O., Deville, E., Negro, F., Chopin, C., & Goffé, B. (2010). Evolution of the
1034 Raman spectrum of carbonaceous material in low-grade metasediments of the Glarus
1035 Alps (Switzerland). Terra Nova, 22(5), 354–360.
1036 Land, L. S. (1998). Failure to precipitate dolomite at 25 °C from dilute solution despite 1000-
1037 fold oversaturation after 32 Years. Aquatic Geochemistry, 4(3), 361–368.
1038 Lascelles, D. F. (2007). Black smokers and density currents: a uniformitarian model for the
1039 genesis of banded iron-formations. Ore Geology Reviews, 32(1–2), 381–411.
1040 Leggett, S. R. (1974). A petrographic and stratigraphic study of the Flaherty Formation, Belcher
1041 Islands, N.W.T. Unpublished B.Sc. Thesis, Brock University, Ontario.

1042 Leri, A. C., Hakala, J. A., Marcus, M. A., Lanzirotti, A., Reddy, C. M., & Myneni, S. C. (2010).
1043 Natural organobromine in marine sediments: new evidence of biogeochemical Br
1044 cycling. Global Biogeochemical Cycles, 24(4).
1045 Liu, D., Yu, N., Papineau, D., Fan, Q., Wang, H., Qiu, X., She, Z., & Luo, G. (2019a). The catalytic
1046 role of planktonic aerobic heterotrophic bacteria in protodolomite formation: Results
1047 from Lake Jibuhulangtu Nuur, Inner Mongolia, China. Geochimica et Cosmochimica
1048 Acta, 263, 31–49.
1049 Liu, D., Xu, Y., Papineau, D., Yu, N., Fan, Q., Qiu, X., & Wang, H. (2019b). Experimental evidence
1050 for abiotic formation of low-temperature proto-dolomite facilitated by clay minerals.
1051 Geochimica et Cosmochimica Acta, 247, 83–95.
1052 Liu, Z. R. R., Zhou, M. F., Williams-Jones, A. E., Wang, W., & Gao, J. F. (2019c). Diagenetic
1053 mobilization of Ti and formation of brookite/anatase in early Cambrian black shales,
1054 South China. Chemical Geology, 506, 79–96.
1055 Liu, D., Fan, Q., Papineau, D., Yu, N., Chu, Y., Wang, H., Qiu, X., & Wang, X. (2020). Precipitation
1056 of protodolomite facilitated by sulfate-reducing bacteria: The role of capsule
1057 extracellular polymeric substances. Chemical Geology, 533, 119415.
1058 Mackenzie, F. T., & Gees, R. (1971). Quartz: synthesis at earth-surface conditions. Science,
1059 173(3996), 533–535.
1060 Maliva, R. G., Knoll, A. H., & Simonson, B. M. (2005). Secular change in the Precambrian silica
1061 cycle: insights from chert petrology. Geological Society of America Bulletin, 117(7–8),
1062 835–845.
1063 Marin-Carbonne, J., Robert, F., & Chaussidon, M. (2014). The silicon and oxygen isotope
1064 compositions of Precambrian cherts: A record of oceanic paleo-temperatures?
1065 Precambrian Research, 247, 223–234.

1066 Mehmood, M., Yaseen, M., Khan, E. U., & Khan, J. M. (2018). Dolomite and dolomitization
1067 model–A short review. International Journal of Hydrology, 2(5), 549–553.
1068 Meister, P., Mckenzie, J. A., Bernasconi, S. M., & Brack, P. (2013). Dolomite formation in the
1069 shallow seas of the Alpine Triassic. Sedimentology, 60(1), 270–291.
1070 Melezhik, V. A., & Hanski, E. J. (2013). Palaeotectonic and palaeogeographic evolution of
1071 Fennoscandia in the Early Palaeoproterozoic. In V. A. Melezhik, A. R. Prave, E. J. Hanski,
1072 A. E. Fallick, A. Lepland, L. R. Kump & H. Strauss (Eds.), The Palaeoproterozoic of
1073 Fennoscandia as Context for the Fennoscandian Arctic Russia - Drilling Early Earth
1074 Project (pp. 111–178). Springer Science & Business Media.
1075 Merino, E., & Canals, À. (2011). Self-accelerating dolomite-for-calcite replacement: Self-
1076 organized dynamics of burial dolomitization and associated mineralization. American
1077 Journal of Science, 311(7), 573–607.
1078 Moore, C. H. (1989). Carbonate diagenesis and porosity (Vol. 46). Elsevier.
1079 Morad, S. (1986). SEM study of authigenic rutile, anatase and brookite in Proterozoic
1080 sandstones from Sweden. Sedimentary Geology, 46(1–2), 77–89.
1081 Noffke, N., Christian, D., Wacey, D., & Hazen, R. M. (2013). Microbially induced sedimentary
1082 structures recording an ancient ecosystem in the ca. 3.48 billion-year-old Dresser
1083 Formation, Pilbara, Western Australia. Astrobiology, 13(12), 1103–1124.
1084 Nutman, A. P., Bennett, V. C., Friend, C. R., van Kranendonk, M. J., & Chivas, A. R. (2016). Rapid
1085 emergence of life shown by discovery of 3,700-million-year-old microbial structures.
1086 Nature, 537(7621), 535–546.
1087 Pacton, M., Ariztegui, D., Wacey, D., Kilburn, M. R., Rollion-Bard, C., Farah, R., & Vasconcelos,
1088 C. (2012). Going nano: a new step toward understanding the processes governing
1089 freshwater ooid formation. Geology, 40(6), 547–550.

1090 Papineau, D., Mojzsis, S. J., Coath, C. D., Karhu, J. A., & McKeegan, K. D. (2005). Multiple sulfur
1091 isotopes of sulfides from sediments in the aftermath of Paleoproterozoic glaciations.
1092 Geochimica et Cosmochimica Acta, 69(21), 5033–5060.
1093 Papineau, D., Walker, J. J., Mojzsis, S. J., & Pace, N. R. (2005) Composition and structure of
1094 microbial communities from stromatolites of Hamelin Pool in Shark Bay, Western
1095 Australia. *Applied and Environmental Microbiology*, 71**,** 4822–4832.
1096 Papineau, D., Mojzsis, S. J., & Schmitt, A. K. (2007). Multiple sulfur isotopes from
1097 Paleoproterozoic Huronian interglacial sediments and the rise of atmospheric oxygen.
1098 Earth and Planetary Science Letters, 255(1–2), 188–212.
1099 Papineau, D. (2010). Global biogeochemical changes at both ends of the Proterozoic: insights
1100 from phosphorites. Astrobiology, 10(2), 165–181.
1101 Papineau, D., De Gregorio, B., Fearn, S., Kilcoyne, D., McMahon, G., Purohit, R., & Fogel, M.
1102 (2016). Nanoscale petrographic and geochemical insights on the origin of the
1103 Palaeoproterozoic stromatolitic phosphorites from Aravalli Supergroup, India.
1104 Geobiology, 14(1), 3–32.
1105 Papineau, D., She, Z., & Dodd, M. S. (2017). Chemically oscillating reactions during the
1106 diagenetic oxidation of organic matter and in the formation of granules in late
1107 Palaeoproterozoic chert from Lake Superior. Chemical Geology, 470, 33–54.
1108 Papineau, D., De Gregorio, B. T., Sagar, J., Thorogate, R., Wang, J., Nittler, L., Kilcoyne, D. A.,
1109 Marbach, H., Drost, M., & Thornton, G. (2019). Fossil biomass preserved as graphitic
1110 carbon in a late Paleoproterozoic banded iron formation metamorphosed at more
1111 than 550° C. Journal of the Geological Society. DOI: 10.1144/jgs2018-097
1112 Papineau, D. (2020). Chemically oscillating reactions in the formation of botryoidal malachite.
1113 American Mineralogist 105, 447–454.

1114 Preston, L. J., Shuster, J., Fernández-Remolar, D., Banerjee, N. R., Osinski, G. R., & Southam, G.
1115 (2011). The preservation and degradation of filamentous bacteria and biomolecules
1116 within iron oxide deposits at Rio Tinto, Spain. Geobiology, 9(3), 233–249.
1117 Pufahl, P. K., & Fralick, P. W. (2004). Depositional controls on Palaeoproterozoic iron formation
1118 accumulation, Gogebic Range, Lake Superior region, USA. Sedimentology, 51(4), 791–
1119 808.
1120 Raiswell, R., & Berner, R. A. (1985). Pyrite formation in euxinic and semi-euxinic sediments.
1121 American Journal of Science, 285(8), 710–724.
1122 Raiswell, R., & Plant, J. (1980). The incorporation of trace elements into pyrite during
1123 diagenesis of black shales, Yorkshire, England. Economic Geology, 75(5), 684–699.
1124 Rasmussen, B., Krapež, B., Muhling, J. R., & Suvorova, A. (2015). Precipitation of iron silicate
1125 nanoparticles in early Precambrian oceans marks Earth's first iron age. Geology, 43(4),
1126 303–306.
1127 Reid, R. P., Visscher, P. T., Decho, A. W., Stolz, J. F., Bebout, B. M., Dupraz, C., Macintyre, I. G.,
1128 Paerl, H. W., Pinckney, J. L., Prufert-Bebout, L., & Steppe, T. F. (2000). The role of
1129 microbes in accretion, lamination and early lithification of modern marine
1130 stromatolites. Nature, 406(6799), 989–992.
1131 Reid, R. P., James, N. P., Macintyre, I. G., Dupraz, C. P., & Burne, R. V. (2003). Shark Bay
1132 stromatolites: microfabrics and reinterpretation of origins. Facies, 49, 299–324.
1133 Ricketts, B. D. (1979). Sedimentology and Stratigraphy of Eastern and Central Belcher Islands,
1134 Northwest Territories. Doctoral Dissertation, Carleton University.
1135 Roberts, J. A., Kenward, P. A., Fowle, D. A., Goldstein, R. H., González, L. A., & Moore, D. S.
1136 (2013). Surface chemistry allows for abiotic precipitation of dolomite at low

temperature. Proceedings of the National Academy of Sciences, 110(36), 14540–14545.

Rogers, J. J. & Santosh, M. (2004). Continents and supercontinents (1st ed.). Oxford University Press.

Schidlowski, M. (2001). Carbon isotopes as biogeochemical recorders of life over 3.8 Ga of Earth history: evolution of a concept. Precambrian Research 106, 117–134.

Schopf, J. W. (1968). Microflora of the Bitter Springs formation, late Precambrian, central Australia. Journal of Paleontology, 651–688.

Schopf, J. W., Kudryavtsev, A. B., Walter, M. R., van Kranendonk, M. J., Williford, K. H., Kozdon, R., Valley, J. W., Gallardo, V. A., Espinoza, C., & Flannery, D. T. (2015). Sulfur-cycling fossil bacteria from the 1.8-Ga Duck Creek Formation provide promising evidence of evolution's null hypothesis. Proceedings of the National Academy of Sciences, 112(7), 2087–2092.

Schulz, H. M., Wirth, R., & Schreiber, A. (2016). Nano-crystal formation of TiO_2 polymorphs brookite and anatase due to organic-inorganic rock-fluid interactions. Journal of Sedimentary Research, 86(2), 59–72.

She, Z. B., Strother, P., & Papineau, D. (2014). Terminal Proterozoic cyanobacterial blooms and phosphogenesis documented by the Doushantuo granular phosphorites II: Microbial diversity and C isotopes. Precambrian Research, 251, 62–79.

She, Z. B., Zhang, Y. T., Liu, W., Song, J., Zhang, Y., Li, C., Strother, P., & Papineau, D. (2016). New observations of ambient inclusion trails (AITs) and pyrite framboids in the Ediacaran Doushantuo Formation, South China. Palaeogeography, Palaeoclimatology, Palaeoecology, 461, 374–388.

1160 Simonson, B. M. (1985). Sedimentology of cherts in the Early Proterozoic Wishart Formation,
1161 Quebec-Newfoundland, Canada. Sedimentology, 32(1), 23–40.
1162 Simonson, B. M. (2003). Origin and evolution of large Precambrian iron formations. In M. A.
1163 Chan, & A. W. Archer (Eds.), Extreme depositional environments: Mega end members
1164 in geologic time, Volume 370 (pp. 231–244). Geological Society of America.
1165 Smith, A.B., Beukes, N.J., Gutzmer, J., Czaja, A.D., Johnson, C.M., and Nhleko, N. (2017)
1166 Oncoidal granular iron formation in the Mesoarchean Pongola Supergroup, southern
1167 Africa: Textural and geochemical evidence for biological activity during iron deposition.
1168 Geobiology, DOI: 10.1111/gbi.12248.
1169 Stirbys, A. F. (1975). A petrographic and geochemical study of the Eskimo Formation, Belcher
1170 Islands, N.W.T. Unpublished B.Sc. Thesis, Brock University, Ontario.
1171 St-Onge, M. R., Wodicka, N., & Ijewliw, O. (2006). Polymetamorphic evolution of the Trans-
1172 Hudson Orogen, Baffin Island, Canada: integration of petrological, structural and
1173 geochronological data. Journal of Petrology, 48(2), 271–302.
1174 Stefurak, E. J., Lowe, D. R., Zentner, D., & Fischer, W. W. (2014). Primary silica granules—A
1175 new mode of Paleoarchean sedimentation. Geology, 42(4), 283–286.
1176 Trower, E. J., & Lowe, D. R. (2016). Sedimentology of the∼ 3.3 Ga upper Mendon Formation,
1177 Barberton Greenstone Belt, South Africa. Precambrian Research, 281, 473–494.
1178 van Maldegem, L. M., Sansjofre, P., Weijers, J. W. H., Wolkenstein, K., Strother, P. K., Wörmer,
1179 L., Hefter, J., Nettersheim, B. J., Hoshino, Y., Schouten, S., Damsté, J. S. S., Nath, N.,
1180 Griesinger, C., Kuznetsov, N. B., Elie, M., Elvert, M., Tegelaar, E., Gleixner, G., &
1181 Hallmann, C. (2019). Bisnorgammacerane traces predatory pressure and the persistent
1182 rise of algal ecosystems after Snowball Earth. Nature Communications, 10(1), 476.

1183 Vandenbroucke, M., & Largeau, C. (2007). Kerogen origin, evolution and structure. Organic
1184 Geochemistry, 38(5), 719–833.
1185 Wacey, D., McLoughlin, N., Kilburn, M. R., Saunders, M., Cliff, J. B., Kong, C., Barley, M. E., &
1186 Brasier, M. D. (2013). Nanoscale analysis of pyritized microfossils reveals differential
1187 heterotrophic consumption in the~ 1.9-Ga Gunflint chert. Proceedings of the National
1188 Academy of Sciences, 110(20), 8020–8024.
1189 Walter, M. R. (Ed.). (1976). Stromatolites (Vol. 20) (1st ed.). Elsevier.
1190 Walter, M.R., Goode, A.D.T., and Hall, W.D.M. (1976) Microfossils from a newly discovered
1191 Precambrian stromatolitic iron formation in Western Australia. Nature, 261, 221–223.
1192 Walter, M. R., Grotzinger, J. P., & Schopf, J. W. (1992). Proterozoic Stromatolites. In J. W.
1193 Schopf (Ed.), The Proterozoic Biosphere: A Multidisciplinary Study. Cambridge
1194 University Press.
1195 Wei, H., Wang, X., Shi, X., Jiang, G., Tang, D., Wang, L., and An, Z. (2019) Iodine content of the
1196 carbonates from the Doushantuo Formation and shallow ocean redox change on the
1197 Ediacaran Yangtze Platform, South China. 322, 160–169.
1198 Weller, O. M., & St-Onge, M. R. (2017). Record of modern-style plate tectonics in the
1199 Palaeoproterozoic Trans-Hudson orogen. Nature Geoscience, 10(4), 305.
1200 Wells, A. J. (1962). Recent dolomite in the Persian Gulf. Nature, 194(4825), 274–275.
1201 Weyl, P. K. (1959). Pressure solution and the force of crystallization: a phenomenological
1202 theory. Journal of Geophysical Research, 64(11), 2001–2025.
1203 Wignall, P. B., Newton, R., & Brookfield, M. E. (2005). Pyrite framboid evidence for oxygen-
1204 poor deposition during the Permian-Triassic crisis in Kashmir. Palaeogeography,
1205 Palaeoclimatology, Palaeoecology, 216(3–4), 183–188.

Williams, H., Hoffman, P. F., Lewry, J. F., Monger, J. W., & Rivers, T. (1991). Anatomy of North America: thematic geologic portrayals of the continent. Tectonophysics, 187(1–3), 117–134.

Zaikin, A. N., & Zhabotinsky, A. M. (1970). Concentration Wave Propagation in Two-Dimensional Liquid-Phase Self-Oscillating System. Nature, 225(5232), 535–537.

Zhang, H. Z., & Banfield, J. F. (2014). Structural characteristics and mechanical and thermodynamic properties of nanocrystalline TiO2. Chemical Reviews, 114(19), 9613–9644.

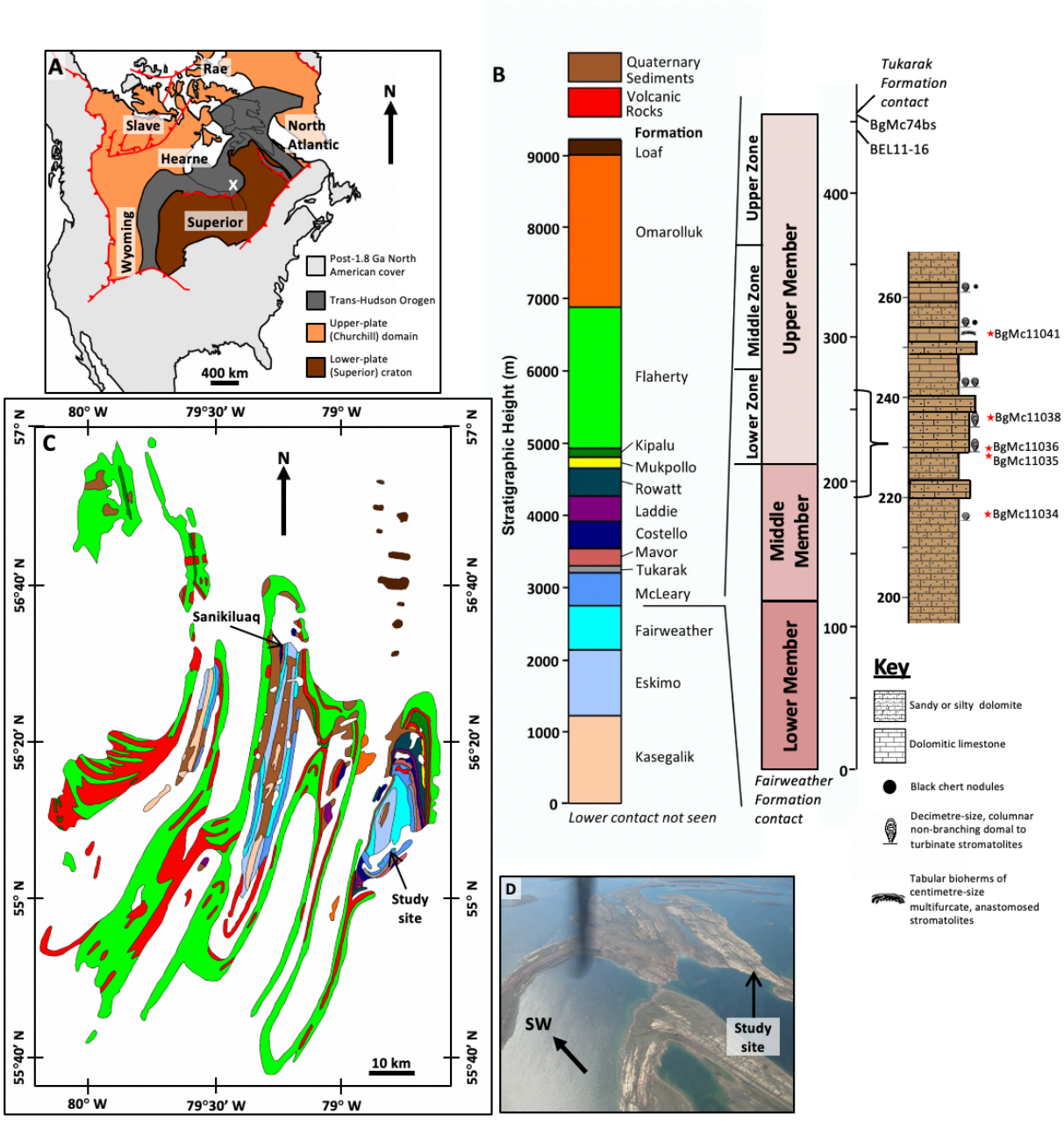

Figure 1: Geological context for this study. A) Geological map of North America with the cratons labelled and a white 'X' showing the location of the Belcher Islands, modified from ***St-Onge et al. (2007)***; B) stratigraphy and colour-coded formations for the Belcher Group and sample positions within the measured cross section of the McLeary Formation (see Table 1); C) geological map of the Belcher Islands; D) aerial photo of the field site of the McLeary Formation.

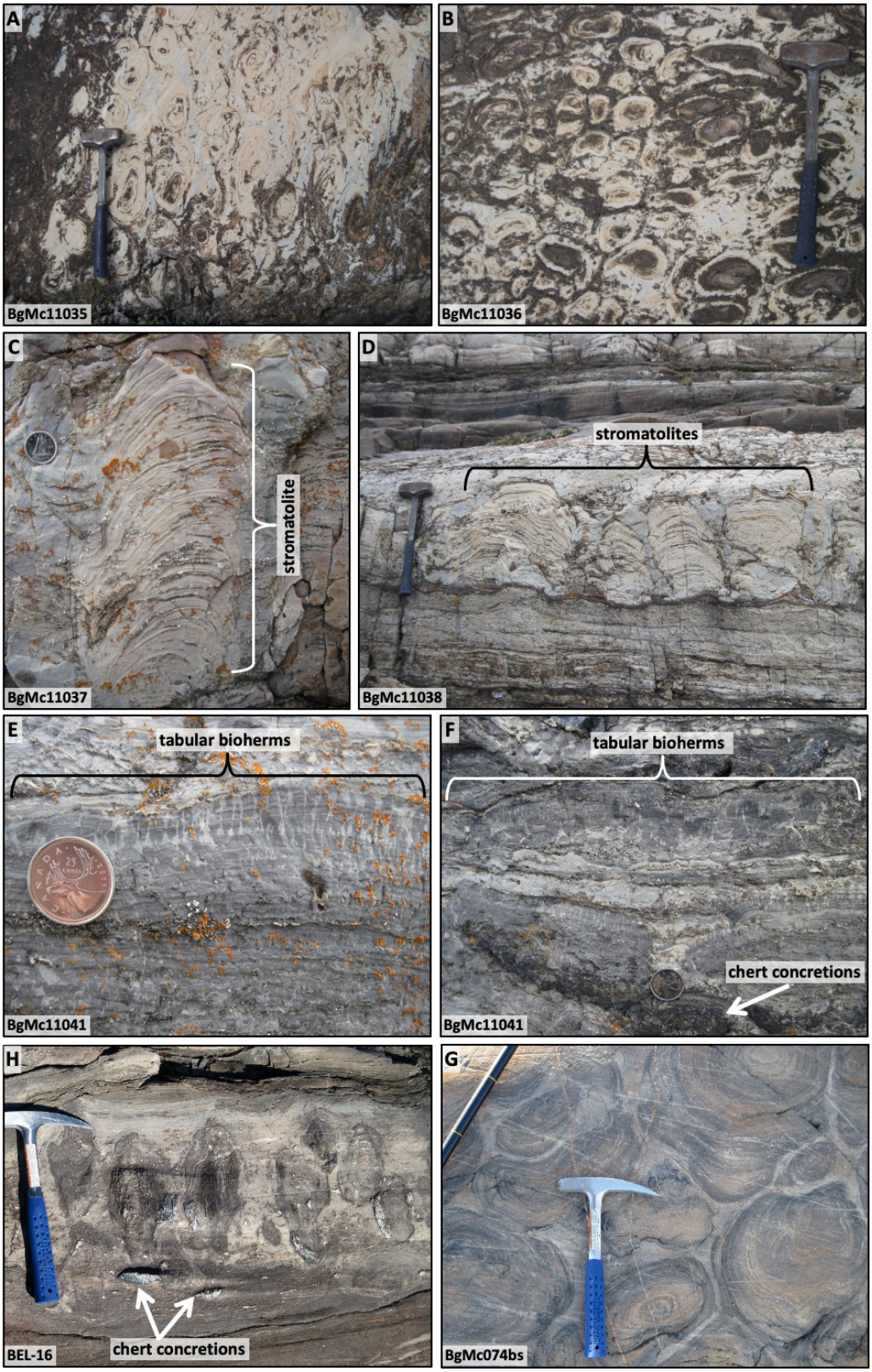

Figure 2: Field outcrop photographs showing various stromatolite morphologies from the McLeary Formation. The captions in the bottom left corner of each image correspond to the thin sections that are at a similar stratigraphic height. A–B) Dolomite outcrops showing horizontal cross sections of decimetre-size, non-branching domal to turbinate stromatolites; C–D) bed of decimetre-size, non-branching, domal to turbinate stromatolites in dolomitic chert; E–F) tabular bioherms of centimetre-size multifurcate, anastomosed stromatolites in chert-rich limestone; G-H) turbinate and bulbous stromatolites, sometimes with multifurcate branching and decimetre-size black chert concretions.

1233

1234

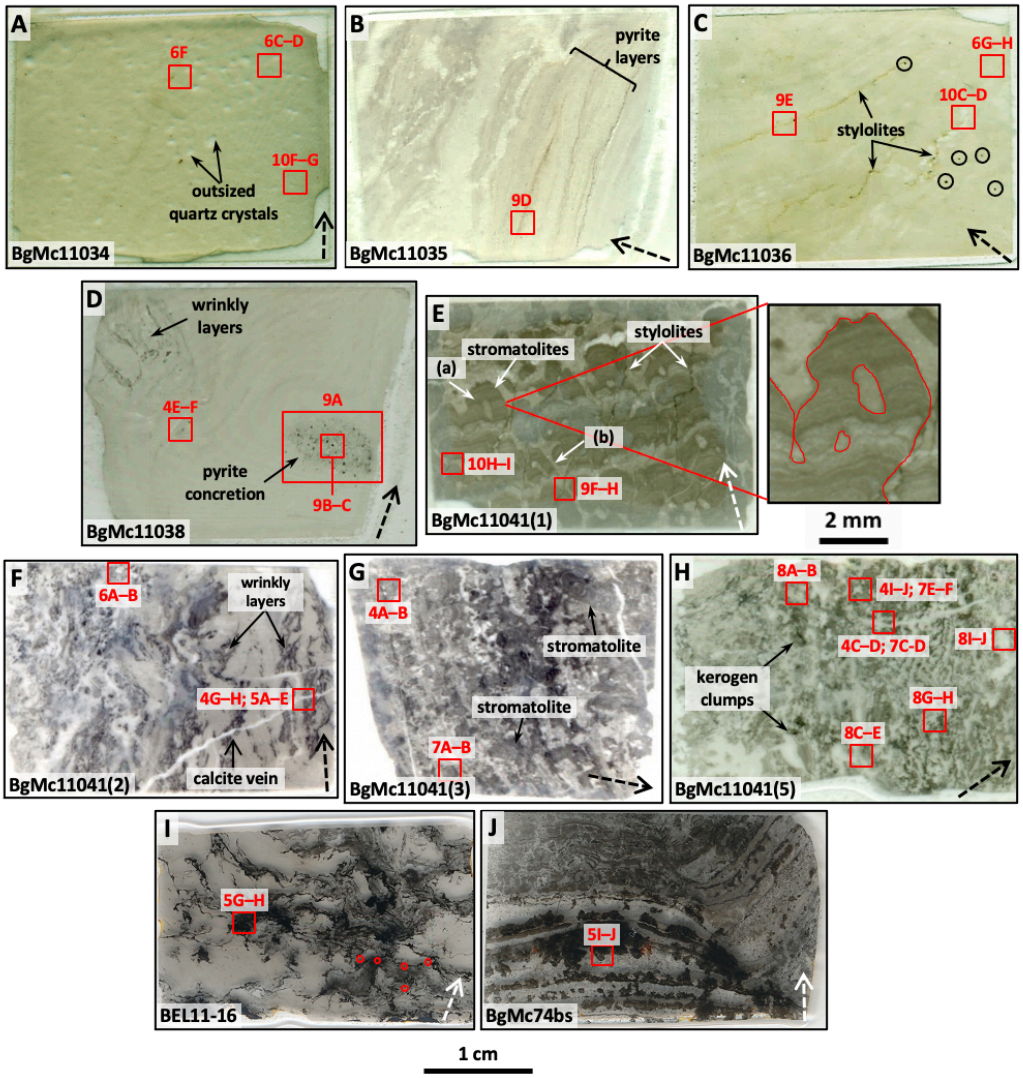

Figure 3: Scans of the thin sections used in this study, arranged in stratigraphic order (low to high). The red numbered squares correspond to the subsequent figures in this study. A) Micritic carbonate with numerous outsized quartz crystals (two crystals are indicated) and no laminations; see Figures 6 and 10; B) micritic carbonate with laminations caused by variations in kerogen content or the amount of pyrite crystals present; see Figure 9; C) micritic carbonate with stylolites and pyrite crystals (black circles) inside a domal stromatolite; see Figures 6, 9, and 10; D) micritic carbonate with a pyrite concretion and undulatory wrinkly layers; see Figures 4 and 9; E) diverse stromatolite morphologies with stylolites between their columns within sparry carbonate; examples of an anastomosed multifurcate column (a) (also shown in higher magnification) and a bifurcate column (b) are highlighted; see Figures 9 and 10; F) carbonate filled with wrinkly layers of probable microbial origin, and calcite veins; see Figures 4, 5, and 6; G) smaller stromatolites preserved in chert; see Figures 4 and 7; H) wrinkly layers of probable microbial origin, and masses of kerogen in chert, carbonate and isopachous quartz; see Figures 4, 7, and 8; I) cherty stromatolite with filamentous clumps of kerogen and groups of filamentous microfossils (in red circles); see Figure 5; J) cherty domal stromatolite; see Figure 5. The dashed arrows in the lower right corner represent the approximate stratigraphic up direction (based on stromatolite morphology) and the scale bar at the bottom is approximately the same for all images.

1235

1236

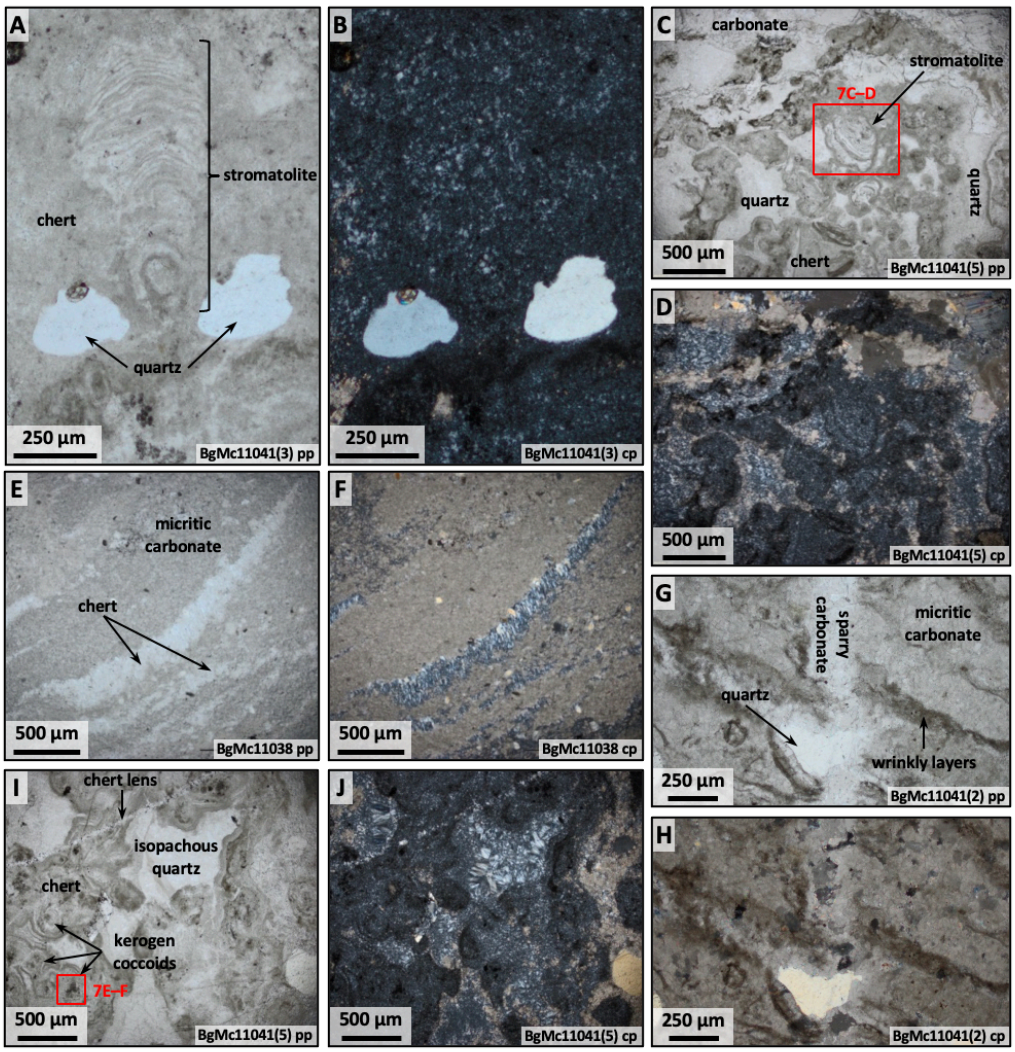

Figure 4: Petrographic textures of microbialites in plane polarised (pp) and cross polarised light (cp). A–B) A turbinate stromatolite preserved in chert with outsized quartz grains at its base; C–D) turbinate-multifurcate stromatolite with a millimetre-size bulbous shape, preserved in chert, the surrounding matrix consists of sparry carbonate, chert and isopachous quartz; E–F) chert lenses of a domal stromatolite in a micritic carbonate matrix; G–H) sparry carbonate cutting across the micritic matrix and wrinkly layers; I–J) chert matrix with isopachous quartz, coarse-grained carbonate, a chert vein and microscopic coccoids. The red numbered squares correspond to the relevant figures.

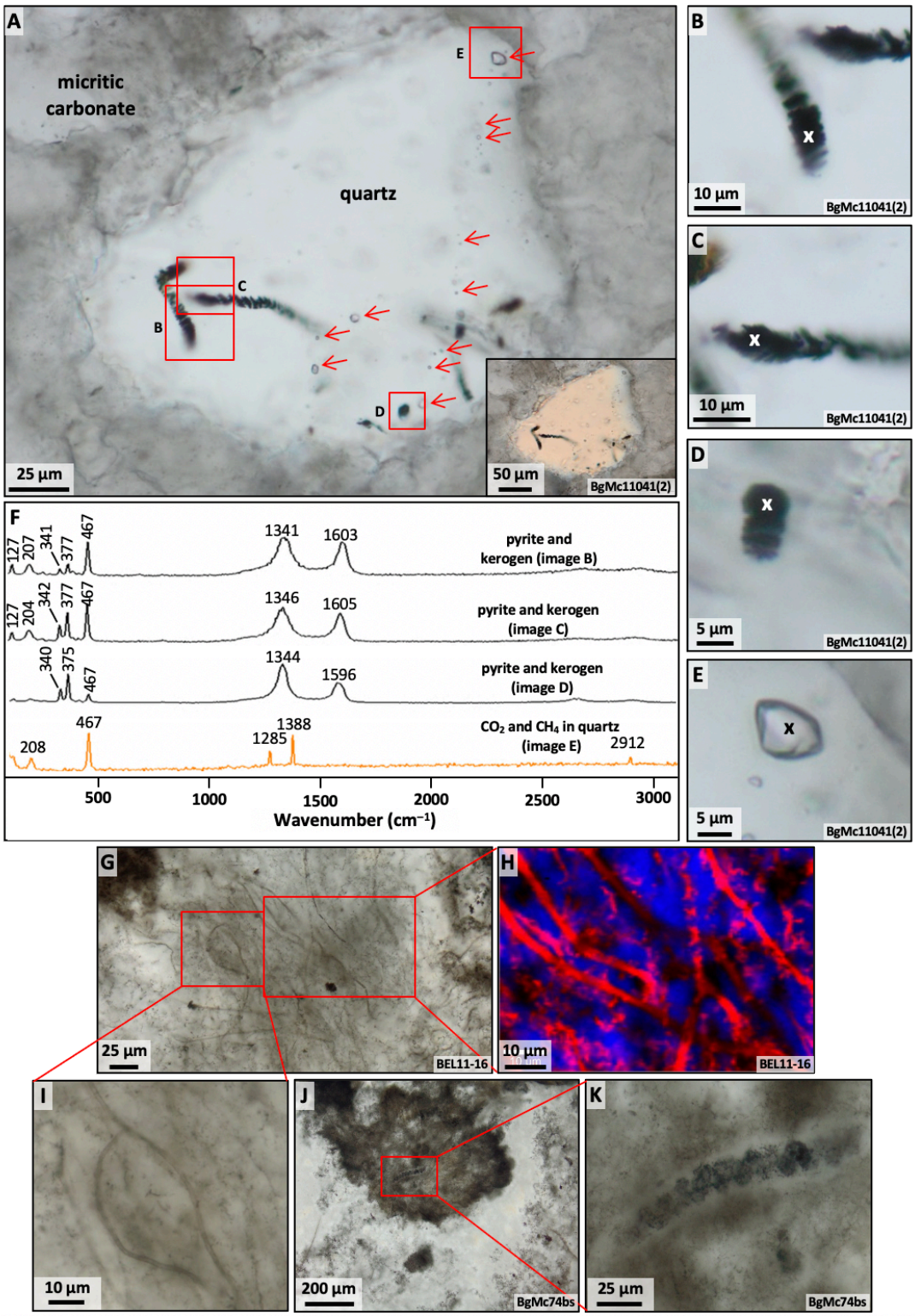

Figure 5: Morphologically distinct filamentous microfossils and fluid inclusions in the McLeary Formation. A) The locations of inclusions in a quartz crystal, the red arrows indicate fluid inclusions, the inset shows the same crystal in cross polarised light and indicates that it is a single crystal; B–D) filamentous microfossils composed of pyrite and kerogen; E) a fluid inclusion containing CO_2 and CH_4; F) Raman spectra for the corresponding structures in the outsized quartz crystal; G) filamentous microfossils in transmitted light; H) Raman image shows that the filaments in G) are composed of kerogen (red) and quartz (blue); I) magnified image of the filaments; J–K) coiled filamentous microfossil composed of dense kerogen nanoscopic particles in a clumps of kerogen.

1244

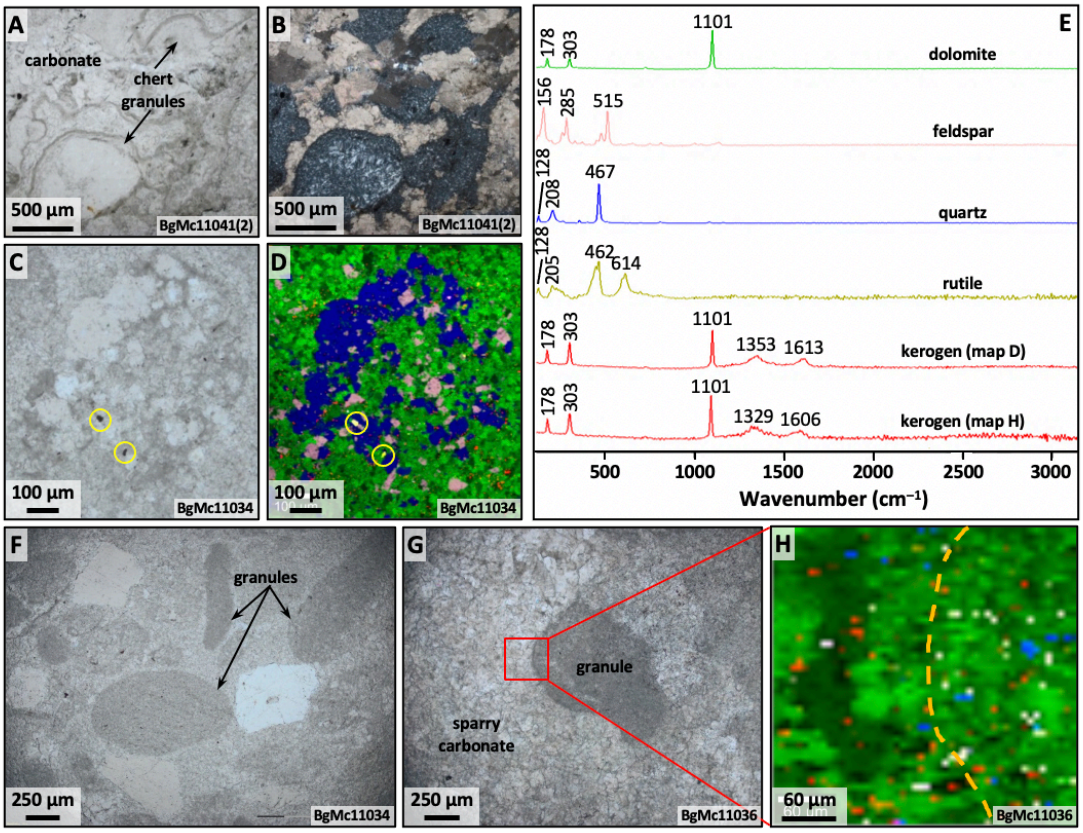

Figure 6: Granules of quartz and carbonate. The colours in the hyperspectral maps correspond to the colours in the Raman spectra. A–B) Chert granules with dark rims, one has isopachous quartz at its centre but the others are composed of just chert; C–D) a granule that contains quartz, feldspar, rutile (circled in yellow) and kerogen; E) Raman spectra for this figure; F) dark sub-ellipsoidal to elongate micritic carbonate granules within a lighter-coloured micritic carbonate matrix; G) irregular-shaped micritic carbonate granule in a sparry carbonate matrix; H) Raman image for the square inset in G) showing a mixture of microscopic inclusions of kerogen, feldspar (coloured white) and quartz in dolomite (with variable peak intensity), the orange dashed line shows the boundary between the granule and the matrix.

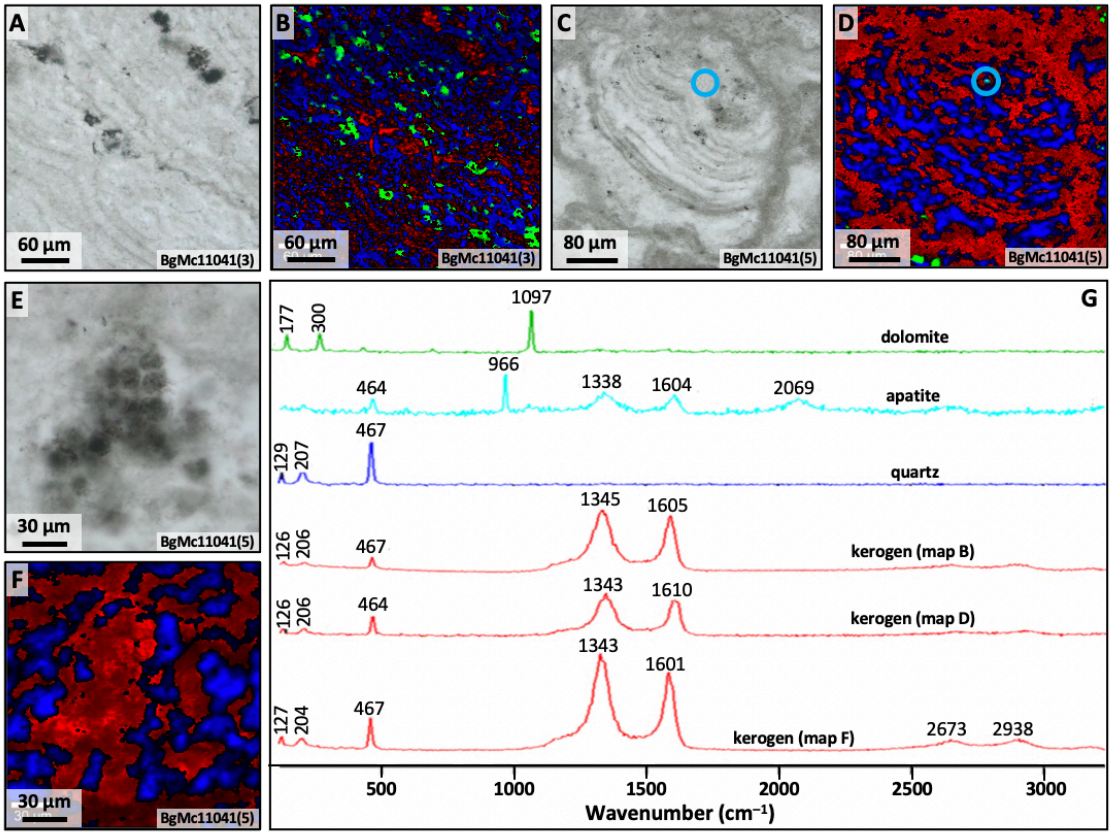

Figure 7: Photomicrographs and Raman maps showing the petrography of organic matter. The colours in the hyperspectral maps correspond to the colours in the Raman spectra. A–D) Kerogen, quartz and carbonate within turbinate stromatolite laminations; C–D) microscopic turbinate-multifurcate stromatolite from Figure 4C with apatite (circled in blue); E–F) kerogen-rich microscopic coccoids in chert; G) Raman spectra for this figure.

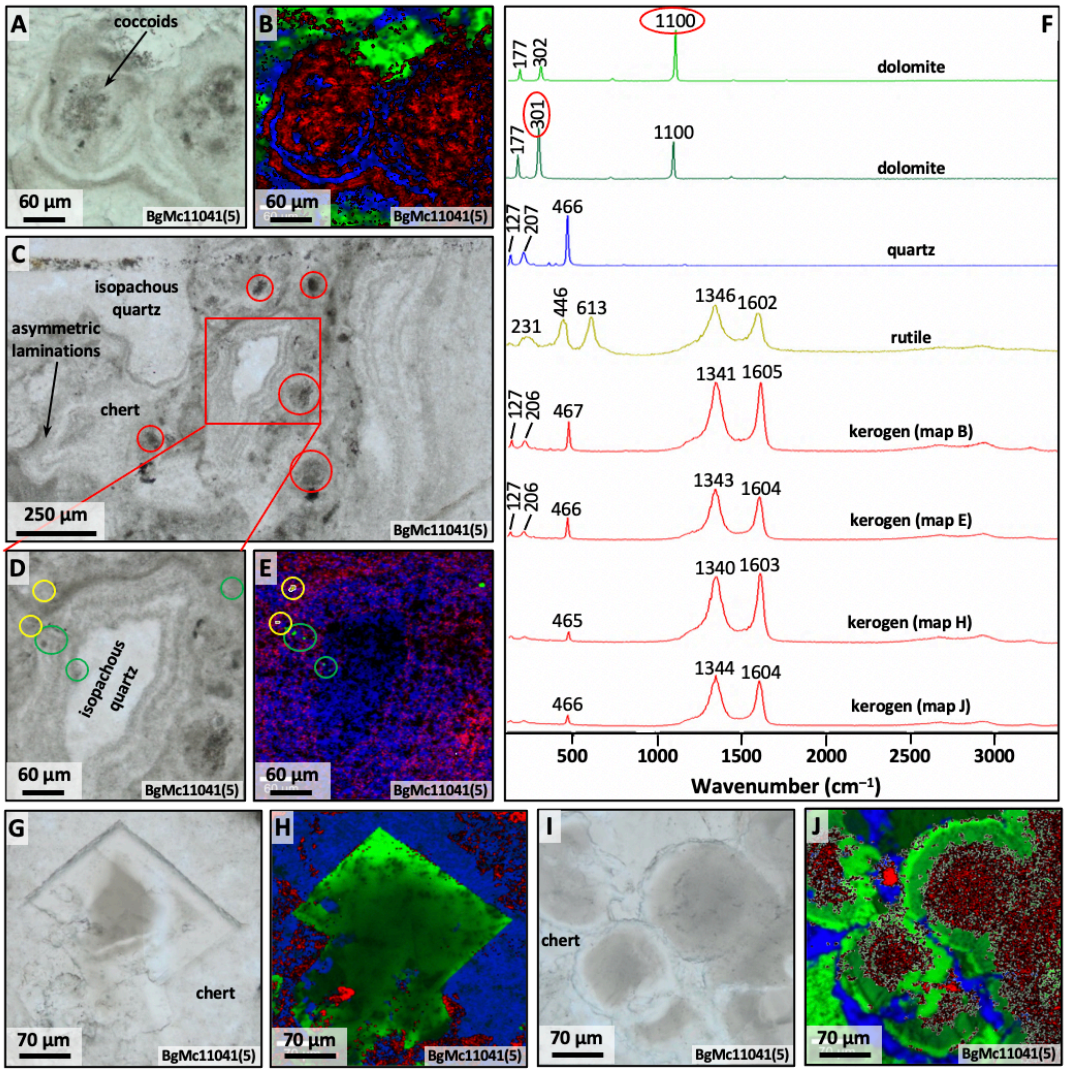

Figure 8: Granules of quartz and carbonate. The colours in the hyperspectral maps correspond to the colours in the Raman spectra. A–B) Chert granules with dark rims, one has isopachous quartz at its centre but the others are composed of just chert; C–D) a granule that contains quartz, feldspar, rutile (circled in yellow) and kerogen; E) Raman spectra for this figure; F) dark sub-ellipsoidal to elongate micritic carbonate granules within a lighter-coloured micritic carbonate matrix; G) irregular-shaped micritic carbonate granule in a sparry carbonate matrix; H) Raman image for the square inset in G) showing a mixture of microscopic inclusions of kerogen, feldspar (coloured white) and quartz in dolomite (with variable peak intensity), the orange dashed line shows the boundary between the granule and the matrix.

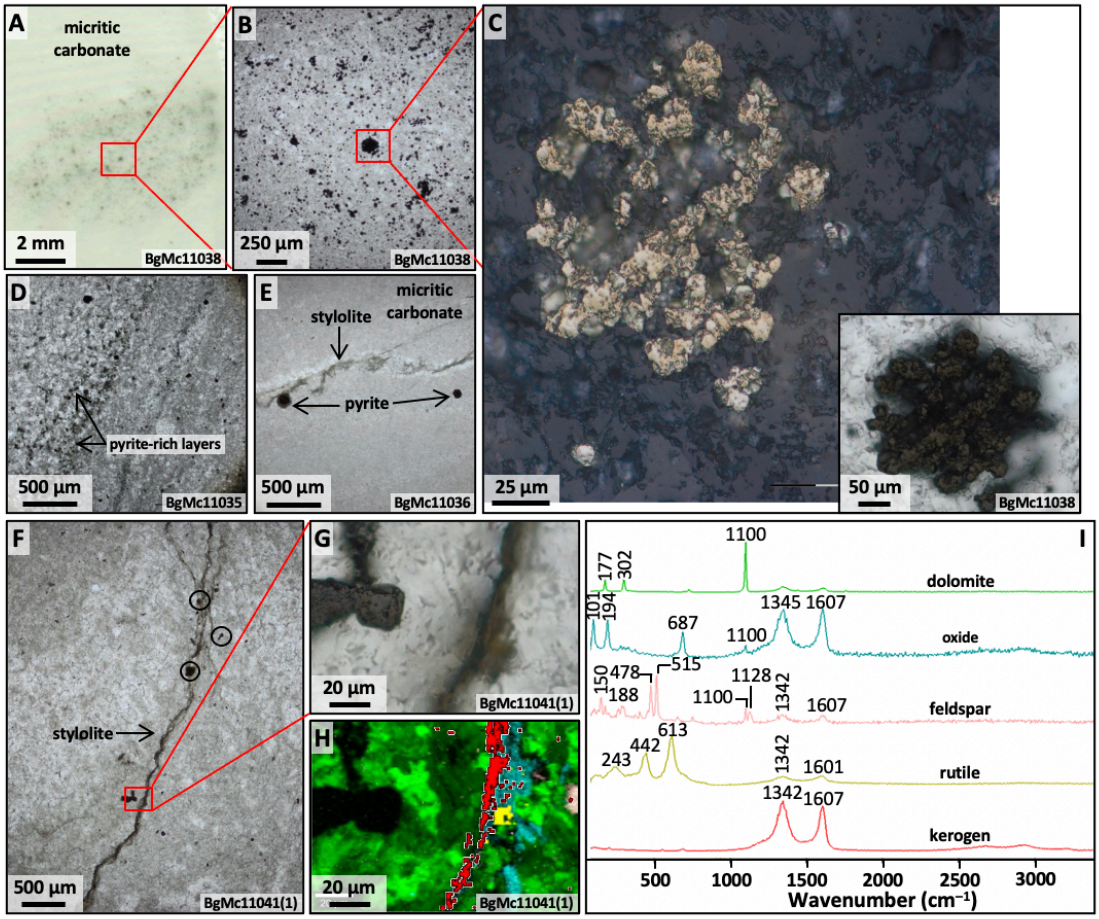

Figure 9: Pyrite in McLeary Formation stromatolites. The colours in the hyperspectral maps correspond to the colours in the Raman spectra. A) A pyrite-rich concretion about 8 mm in length; B) higher magnification of A) shows that the concretion contains several pyrite framboids in micrite as well as disseminated quartz visible as clear crystals; C) high magnification of a pyrite framboid in reflected light showing that it is composed of several microscopic pyrite euhedral crystals; D) pyrite-rich layers in micritic carbonate; E) Two pyrite crystals in close proximity to a stylolite; F) a stylolite with several pyrite crystals along its length (a few are highlighted with black circles); G) the inset in F); H) a micro-Raman image of G); I) Raman spectra for this figure.

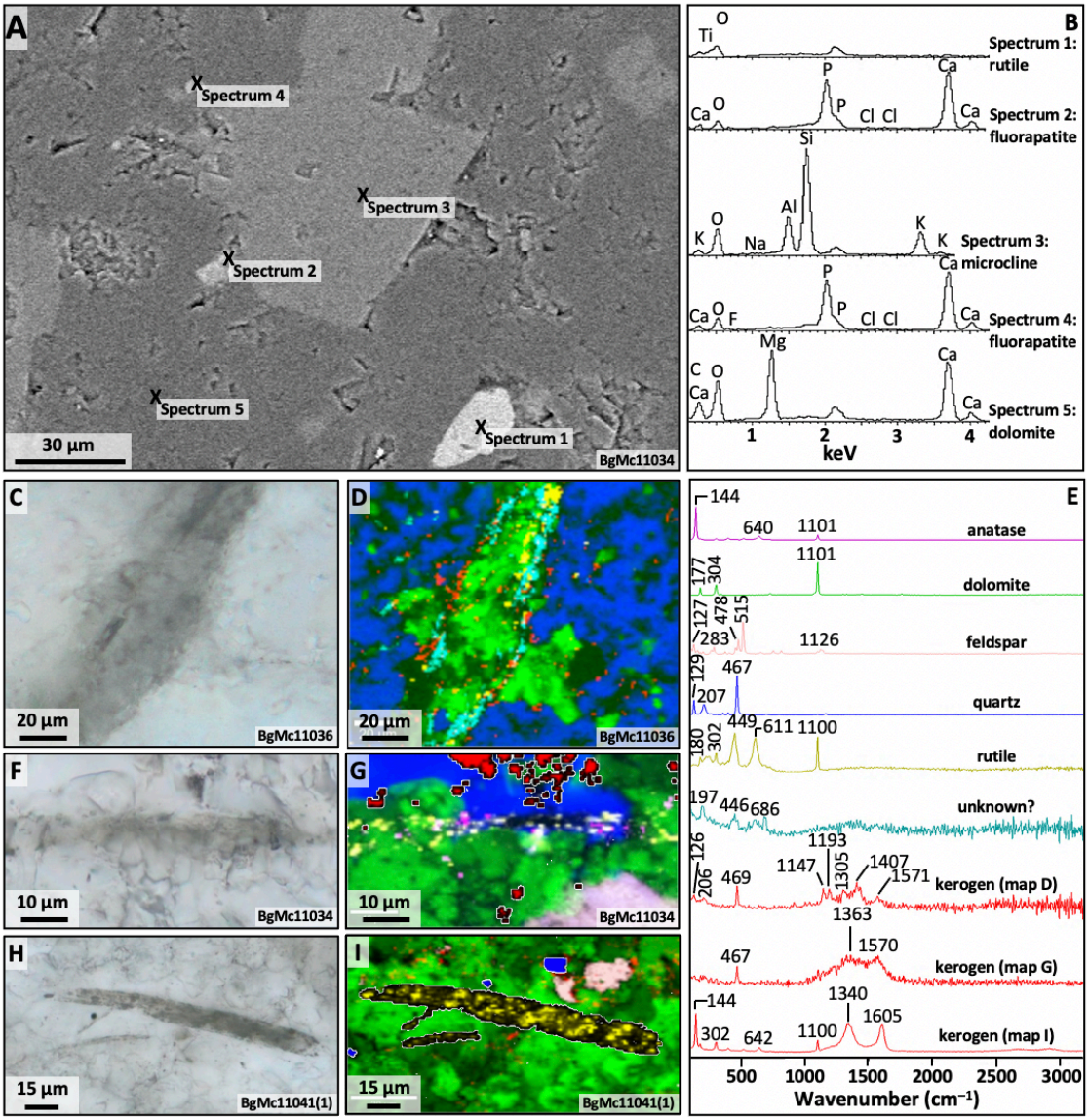

Figure 10: Accessory minerals in carbonate matrix. The colours in the hyperspectral maps correspond to the colours in the Raman spectra. A) Backscattered image of SEM showing small grains of rutile and fluorapatite and a larger grain of microcline within micritic dolomite; B) SEM spectra for the map A) (the unlabelled peaks around 2 keV were produced by the gold coating on the thin section); C–D) part of a stylolite that contains various minerals; E) Raman spectra for this figure; F–I) photomicrographs of rutile needles.

9. Tables

Table 1: Formations of the Belcher Group ***(after Rickets, 1979, and this work)***.

Formation	Thickness (m)	Description	Palaeoenvirontment	Stromatolite Morphologies
Loaf	220	Red and grey cross-bedded arkoses and mudstones	Fluvial	N/A
Omarolluk	2105	Well-bedded greywackes and shales, typical Bouma cycles; minor flattened carbonate boulders (concretionary-like) filling channels; dewaterting structures, concentric concretions; thin tuffs near base	Shallow-water fluviatile; submarine fan complex	N/A
Flaherty	250–1950	Tholeiitic basalts (massive flows, pillowed flows and columnar basalt); variety of volcaniclastics: thinly bedded tuffs, pyroclastic turbidites, massive pyroclastic beds (predominantly hyaloclastite, black shale, and massive calcite); Haig Sills	N/A	N/A
Kipalu	105–125	Fe-silicate Banded Iron Formation, lenses of granular jasper	Below the wave base (high-energy environment)	N/A
Mukpollo	40–145	Cross-bedded quartz arenites, siltstones	Intertidal to shallow subtidal	N/A

Rowatt	290–390	Upper Member: brecciated grainstones, dolostones, karst infilled by multi-coloured chert; Lower Member: variety of sandstones, mudstones with isolated carbonate buildups	Intertidal to mudflat with prolonged aerial exposure	Sub-cylindrical, non-branching
Laddie	230–350	Red and green argillites and shales	Below the storm wave base	N/A
Costello	240–370	Red and green argillites with dolomite concretions; carbonate rhymites, minor allodapic calcarenites, slump structures	Below the storm wave base	N/A
Mavor	90–245	Stromatolitic dolostones; laminated dolostone	Subtidal to storm wave base; intertidal	Columnar and domal, with digitate branching
Tukarak	40–93	Upper Member: ribbon rock, stromatolitic dolostones; Lower Member: fine sandstones, stone rosettes	Shallow subtidal (above wave base)	Columnar
McLeary	365–455	Upper Member: stromatolitic dolostones; Middle Member: dolarenites, lutites, beachrock; Lower Member: dolostone, abundant stone rosettes; Beachrock Marker Bed at base	Shallow subtidal; intertidal; tidal flat; mud flat; hypersaline supratidal	Domal with no lateral linking; columnar with furcate branching; conical; turbinate with lateral linking
Fairweather	356–610	Upper Member: sandstones, siltstones, channels; Lower Member: pisolitic dolostones, desiccated	Tidal flats with channels; intertidal; supratidal	N/A

			mudstones, sandstones		
	Eskimo	0–910	Tholeiitic basalts (massive flows, rare pillows, thin volcaniclastics)	N/A	N/A
	Kasegalik	1220	Stromatolitic dolostones; red mudstones, halite and sulphate casts	Supratidal; shallow subtidal	Domal; furcate brancing

Table 2: Stable isotope composition of organic matter and carbonate from the studied samples.

Sample name	GPS coordinates	Rock type	Position in section (m)*	TOC (%wt)	$\delta^{13}C_{org\text{-}PDB}$ (‰)	$\delta^{13}C_{carb\text{-}PDB}$ (‰)	$\delta^{18}O_{carb\text{-}PDB}$ (‰)	$\delta^{18}O_{carb\text{-}SMOW}$ (‰)
BgMc11034	56°06'24.3" N 78°50'01.5" W	coarse laminated silty dolomite	221.5	0.23	-27.1	0.0	-7.9	+22.8
BgMc11035		decimetre size dolomitic columnar stromatolite	228.5	0.07	-22.9	-0.5	-11.1	+19.5
BgMc11036		decimetre size dolomitic columnar stromatolite	229.5			-0.4	-7.2	+23.5
BgMc11038		decimetre size dolomitic columnar stromatolite	237.0	0.14	-26.1	-0.5	-8.3	+22.3
BgMc11041	56°06'20.6" N 78°50'01.7" W	dolomitic tabular bioherms of cm size multifurcate stromatolites	252.7	0.31	-29.4	0.0	-8.4	+22.2
BgMc74bs	56°05'59" N 78°49'14.9 W	domal stromatolites in cherty dolostone						
BEL11-16		domal cherty stromatolite	462.0	0.06	-26.5			

* The contact with the top of the Fairweather Formation in this section is at 61m. One standard deviation variations on standards analysed during these sessions are respectively 0.3, 0.1 and 0.1 ‰ for $\delta^{13}C_{org}$, $\delta^{13}C_{carb}$, and $\delta^{18}O_{carb}$.

Table 3: Raman spectral parameters (in cm^{-1}) of kerogen in the cherty stromatolitic dolomite from the McLeary Formation. The geothermometer calculations are based on ***Lahfid et al. (2010)***.

		D1 Band			D2 Band			G Band			D3 Band			D4 Band			Geothermometer			
Sample #	**Figure**	**Position**	**FWHM**	**Area**	**Position**	**FWHM**	**Area**	**Position**	**FWHM**	**Area**	**Position**	**FWHM**	**Area**	**Position**	**FWHM**	**Area**	**RA1**	**RA2**	**RA1-T (°C)**	**RA2-T (°C)**
BgMc11041(2)	**Figure 5B**	1344	70	2500	1620	22	200	1602	35	1000	1510	300	800	1245	200	700	0.6154	1.6000	299	296
BgMc11041(2)	**Figure 5C**	1344	60	1280	1618	26	125	1600	37	432	1510	210	230	1245	200	200	0.6528	1.8806	346	358
BgMc11041(2)	**Figure 5D**	1345	45	6800	1620	22	550	1595	37	2700	1510	330	2500	1245	200	3000	0.6302	1.7043	318	319
BgMc11034	**Figure 6D**	1347	72	3900	1615	22	370	1602	45	1100	1515	320	2000	1245	200	800	0.5753	1.3545	249	241
BgMc11041(3)	**Figure 7B**	1344	79	13,750	1615	33	2400	1598	43	4750	1510	200	500	1245	70	500	0.6507	1.8627	344	354
BgMc11041(5)	**Figure 7D**	1344	75	2100	1622	45	300	1595	38	800	1510	300	250	1245	200	200	0.6301	1.7037	318	319
BgMc11041(5)	**Figure 7F**	1344	70	9500	1619	42	2500	1595	45	3500	1510	250	650	1245	100	750	0.6065	1.5414	288	283
BgMc11041(5)	**Figure 8B**	1344	70	12,500	1622	22	1000	1599	34	6050	1510	250	4000	1245	200	3000	0.5838	1.4027	260	252
BgMc11041(5)	**Figure 8E**	1344	69	22,000	1615	34	5000	1599	30	5750	1520	150	3000	1245	100	3000	0.6452	1.8182	337	344
BgMc11041(5)	**Figure 8H**	1342	70	10,000	1620	36	1800	1602	34	3900	1515	175	2000	1245	160	2000	0.6091	1.5584	292	286
BgMc11041(5)	**Figure 8J**	1343	54	7500	1617	30	1475	1602	30	2700	1515	200	1750	1245	125	1250	0.5963	1.4768	276	268
BgMc11041(1)	**Figure 9H**	1344	77	23,500	1616	34	4500	1600	34	6200	1510	250	7500	1245	100	2000	0.5835	1.4011	260	251
BgMc11041(1)	**Figure 10I**	1344	76	10,500	1616	30	1575	1602	30	2900	1516	240	4000	1245	100	1000	0.5757	1.3569	250	242
																		Average	**295**	**297**
																		1σ	**35**	**42**